CMOS-Based Electrokinetic Microfluidics With Multi-Modal Cellular and Bio-Molecular Sensing for End-to-End Point-of-Care System

Chengjie Zhu, *Graduate Student Member, IEEE*, Jesus Maldonado, and Kaushik Sengupta, *Senior Member, IEEE*

***Abstract*—The importance of point-of-care (POC) bio-molecular diagnostics capable of rapid analysis has become abundantly evident after the outbreak of the Covid-19 pandemic. While sensing interfaces for both protein and nucleic-acid based assays have been demonstrated with chip-scale systems, sample preparation in compact form factor has often been a major bottleneck in enabling end-to-end POC diagnostics. Miniaturization of an end-to-end system requires addressing the front-end sample processing, without which, the goal for low-cost POC diagnostics remain elusive. In this paper, we address bulk fluid processing with AC-osmotic based electrokinetic fluid flows that can be fully controlled, processed and automated by CMOS ICs, fabricated in TSMC 65 nm LP process. Here, we combine bulk fluid flow control with bio-molecular sensing, cell manipulation, cytometry, and separation—all of which are controlled with silicon chips for an all-in-one bio-sensing device. We show CMOS controlled pneumatic-free bulk fluid flow with fluid velocities reaching up to 160 μm/s within a microfluidic channel of 100 $\times$ 50 μm^2 of cross-sectional area. We incorporate electrode arrays to allow precise control and focused cell flows (± 2 μm precision) for robust cytometry, and for subsequent separation. We also incorporate a 16-element impedance spectroscopy receiver array for cell and label-free protein sensing. The massive scalability of CMOS-driven microfluidics, manipulation, and sensing can lead to a new design space and a new class of miniaturized sensing technologies.**

***Index Terms*—AC osmosis, biosensing, cell separation, CMOS, cytometry, dielectrophoresis, electrokinetics, hydrodynamic focusing, impedance spectroscopy, protein sensing, osmosis.**

I. Introduction

THE widespread of the COVID-19 pandemic has demonstrated, without any reservations, the importance of POC diagnostics that allow an end-to-end biosensing capability from bio-sample to diagnostic information [1]. Bridging this sample-to-information paradigm requires addressing two broad and equally important objectives that need to satisfy the sensitivity and specificity requirements, while being low cost that is necessary for POC applications. The first objective is to automate the first step in the biosensing process that involves extracting and processing the relevant bio-samples (cells/molecules) selectively. Such sample preparation can involve several steps including dissolution and mixing with several reagents, dilution, and filtering, all of which are critical to the robustness of the assay chemistry, sensing sensitivity and specificity [2].

The second step involves the detection of the desired substances (cells and molecules of interest) in the processed sample. In the past decade, there have been significant efforts in enabling such low-cost sensing devices. These include quantitative platforms using CMOS-based integrated circuit technologies. Several modalities of bio-molecular sensing including fluorescence-based, magnetic-based, label-free sensing have been demonstrated in prior works across both nucleic acid and protein-based assays [3]–[11]. For cells, cytometry has also been demonstrated with magnetic-labels or in a label-free manner [12], [13].

On the other hand, sample preparation is still typically done either manually or with an array of pressure-driven microfluidic channels, connected through a set of tubes to syringe pumps (Fig. 1). As a result, while the sensing interface is miniaturized, the rest of the system can still be bulky and expensive, thereby severely liming its range of applications (Fig. 1). In the case of ingestible-based electronics for in-vivo sensing [4], [14], such pressure driven flow is even more impractical, given the ultra-miniaturized nature of the entire sensing system. Therefore, electronically driven flow becomes attractive to consider, given its scalability and compatibility with the chip-scale sensing interfaces. While electrically driven droplets, molecular and cell manipulation techniques, such as electro-wetting, electrophoresis, dielectrophoresis and surface acoustic wave have been demonstrated in piror works [15]–[18], they do not have the capability to process bulk bio-sample fluids or require discrete components that is not integrated in a single sensing substrate while performing cytometry and bio-molecular sensing.

In this work, we present a CMOS-based bio-sensing system that combines the functionalities of bulk fluid processing and cellular/bio-molecular sensing capabilities in a single hand-held platform (Fig. 2) [19]. We demonstrate, for the first time, a CMOS-microfluidic biosensing system that is capable of 1) driving bulk electrolyte fluid with AC electro-osmosis, 2) cell manipulation and separation with dynamic electric field manipulations through an array of electrodes, 3) cytometry and label-free bio-molecular sensing with 16-element integrated

Manuscript received August 24, 2021; revised November 25, 2021; accepted December 5, 2021. Date of publication December 16, 2021; date of current version February 16, 2022. This paper was recommended by Associate Editor M. Ghovanloo. *(Corresponding author: Chengjie Zhu)*

The authors are with the Electrical Engineering, Princeton University, Princeton, NJ 08540 USA (e-mail: chengjie@princeton.edu; jmalvaz@princeton.edu; kaushiks@princeton.edu).

Color versions of one or more figures in this article are available at https://doi.org/10.1109/TBCAS.2021.3136165.

Digital Object Identifier 10.1109/TBCAS.2021.3136165

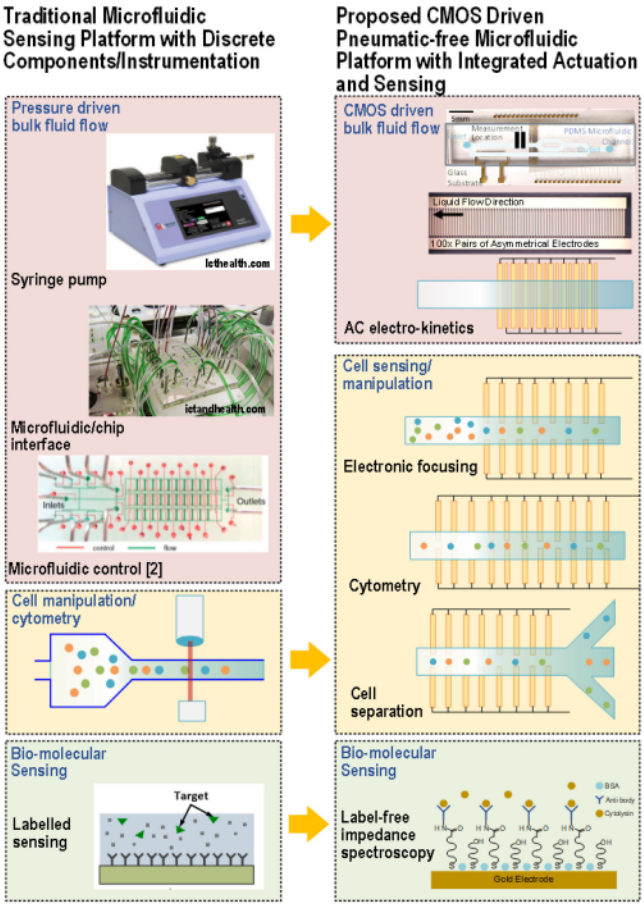

Fig. 1. A comparison figure between traditional and proposed mirofluidic sensing platforms. In traditional microfluidic platforms (left), components are discrete and it requires bulky instrumentation such as pneumatic pumps, complex microlfuidic tubing and optical-based cytometry sensing. The proposed CMOS driven microfluidic platform (right) has the capability to perform pneumatic-free bulk fluid driving with integrated cell sensing/actuation as well as label-free bio-molecular sensing on a single platform.

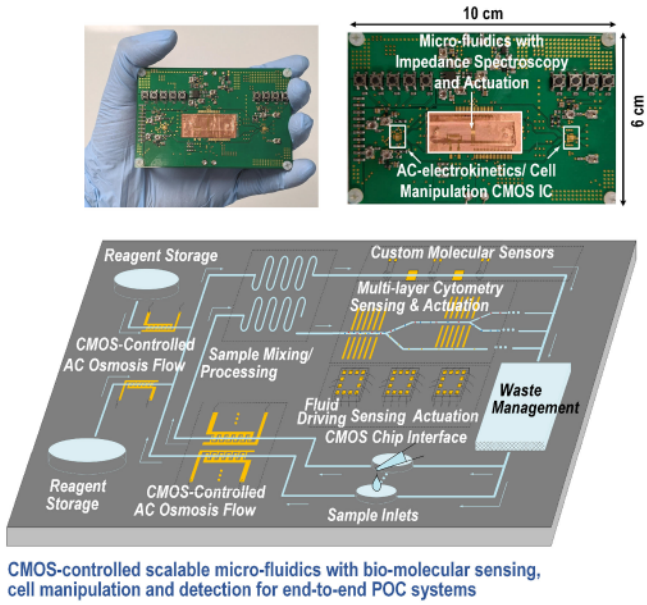

Fig. 2. A conceptual diagram of CMOS-based microfluidics and biosensing system. We combine 1) CMOS driven scalable microfluidics with controlled AC-osmotic flow, 2) cell manipulation, sensing and separation through dynamic electric field synthesis, and 3) impedance spectroscopy for cytometry and bio-molecular sensing.

impedance spectroscopic receivers. While we demonstrate these kernel functionalities in a multi-chip module, the overall architecture, microfluidics and sensing components can be massively scaled up for various POC applications due to the elimination of pressure-driven flows. Such flows can allow enhancement of detection sensitivity [20]–[23], and enable further automation of sample preparation, mixing with reagents, all of which are carried out with CMOS ICs and can be potentially used by non-experts in resource-limited settings. Fig. 2 is meant to capture the vision of a CMOS-driven and controlled and sensing system in an end-to-end fashion.

The paper is organized as follows. Section II describes the fundamental principles of the electro-osmotic flows, particularly focusing on AC-osmosis for bulk fluid flow, and its compatibility with CMOS-based driving systems for realization of pneumatic-free microfluidics. The section also discusses electronic focusing of cells, cytometry and separation with electrode arrays. Section III focuses on electrode fabrication and microfluidic packaging. Section IV elaborates on the impedance spectroscopy architecture, and constituent circuits. Section V presents the measurements results followed by conclusion.

II. Electrokinetics: AC Osmotic Bulk Fluid Flow With CMOS ICs

Pneumatic-based microfluidic flow with syringe pumps is challenging to scale up due to the complexity and increasing number of pneumatic pumps and microfluidic tubing required for sample preparation in biosensing systems. Electrokinetics can provide a scalable solution through controlling of ionic fluids with electric fields. While the details of the physics of the motion are beyond the scope of the paper [24], here, we focus on AC osmosis that allows scalable electrolyte motion with the voltage levels supported by CMOS ICs.

A. Fundamentals of Electro-Osmotic Flow

Electro-osmosis provides one of the most popular non-pressure driven flows in microfluidics. The basic principle of the nonlinear flow generated by electro-osmosis relies on a charged electrode that creates non-neutral ionic layers at the electrode-electrolyte interface. Within the interface, a cloud of charged particles creates a diffusion layer, which under the influence of an external electric field, drags the polarizable water molecule tangential to the electrode surface causing the bulk fluid motion [24].

The design principle for the electrodes that create the desired osmotic flow, therefore, focuses on engineering the optimal electric fields that generate the nonlinear drag force to allow net fluid flow in one direction. When a charged electrode surface comes in contact to an ionic solution, electrode double-layer forms. Fig. 3

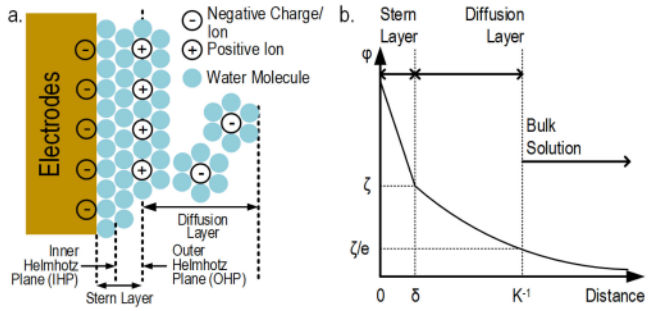

Fig. 3. A microscopic view of the electrode-electrolyte double-layer interface. (a) Stern layer, where ions are relatively immobile and diffusion layer, where ions are free to move. (b) Corresponding electric potential profile showing exponentially decreasing potential in the diffusion layer.

demonstrates a microscopic view at the electrode-electrolyte double-layer interface. Close to the electrode, a tightly bound stern layer forms including an inter (IHP) and outer Helmholtz plane (OHP) [25] (Fig. 3). Beyond the tightly bound stern layer, the potential decreases exponentially creating a cloud of charges that attract the polarizable water molecules, known as the diffusion layer. The exponentially decreasing potential profile can be modeled through Debye-Huckle theory approximation [25]. In addition, due to the non-uniform charge distribution, there exists a net electric field in the double-layer, which can be modeled with an equivalent capacitance, C_{DL}. The value of the capacitance per unit area is inversely proportional to the diffusion length (κ^{-1}) [25]–[27], where κ^2 given by $\kappa^2 = \frac{q^2}{\epsilon k_B T}[\Sigma n_i z_i^2]$, and q is the charge of a single electron. ϵ is the dielectric constant of the medium. k_B is Boltzmann's constant. T is temperature in kelvin. n_i represents the number of charges for each ion type in a unit volume and z_i is the valency of each ion. As an example, in 0.001× PBS solution, the debye length contributed by the dominated ions, Na+ and Cl- ($\approx$ 0.137 mM for each ion), alone is roughly around 20-30 nm.

In summary, the various principles of the electro-osmosis can be itemized as follows

- Ions in the diffusion layer attract the polarizable water molecules. Therefore, by moving the ions in the diffusion layer, there will be a drag effect on the water molecules that eventually lead to bulk fluid motion.
- Manipulation of the ions in the diffusion layer can be realized by creating tangential electric fields close to the electrode surface.
- Presence of ions is necessary for such fluid motion. Many bio-samples (blood/saliva/sweat) are ionic, and therefore, such techniques are applicable. However, a very high ionic concentration can create a small diffusion lengths (κ^{-1}) impeding such fluid motion [22]. More discussions regarding driving high ionic solution ($>$ 100mM) will be addressed in later sections.

B. AC Electro-Osmotic Flow

While the previous description provides a general guidance of nonlinear electro-osmotic flow, AC osmosis provides one possible mechanism to induce the electric fields (Fig. 4). Electro-osmotic flow can be induced with a DC field. However, in this case, the required voltage in DC osmosis is directly proportional to the separation distance between the electrodes. This can reach to hundreds of volts when the channel length, and therefore, the separation electrodes extend beyond 100 μm. This makes such bulk fluid drivers non-scalable [22].

On the other hand, AC osmosis relies on laterally positioned asymmetric electrode pairs, lowering the voltage requirements that can be handled by CMOS ICs. As shown in Fig. 4, to ensure that the bulk fluid travels uni-directionally, AC electro-osmosis takes the advantage of the asymmetric nature of the electrode design to generate an AC tangential electric field profile that eventually contributes to bulk fluid motion [28]–[32].

In addition to producing a net bulk fluid flow within the channel, AC electro-osmosis can be also deployed as active fluid mixer through symmetrical electrode designs. This is particularly useful to increase sensitivity for bio-molecular detection in microfluidic channels to bring sensing target in the bulk fluid closer to the sensor site through local fluid vortex, therefore significantly extending the limit of detection within a limited time frame, compare to diffusion-based bio-molecular binding [21]–[23].

C. Electrode Design and Bulk Fluid Flow

As shown in Fig. 4(a)–(b), the interaction of the asymmetric electrodes with the electrolyte solution can be represented by an equivalent circuit model at the electrode-electrolyte interface [32]. Here, C_{DL} represents the double-layer capacitance and R_1 to R_N represent the bulk fluid resistance ($R_1 > R_N$) for each current path. To calculate the tangential electric field to quantify the fluid flow, one can calculate the voltage difference between V_N and V_1, as shown in Fig. 4(a). It can be shown that this tangential field due to the voltage difference between V_N and V_1 behaves with a standard second-order band-pass response, with the peak amplitude occurs at the center frequency ω_o

$$V_t = V_N - V_1 = \frac{jA_o\frac{\omega}{\omega_o Q}}{1 + j\frac{\omega}{\omega_o Q} - (\frac{\omega}{\omega_o})^2}V_{AC} \tag{1}$$

where $A_o = C_{DL,S}(R_N - R_1)/(R_1 + R_N)(C_{DL,L} + C_{DL,S})$, $Q = \sqrt{R_1 R_N}/(R_1 + R_N)(C_{DL,L} + C_{DL,s})$ (quality factor) and $\omega_o = (C_{DL,L} - C_{DL,s})/(C_{DL,S}C_{DL,L}\sqrt{R_1 R_N})$. In addition, the absolute voltage at V_N is larger than V_1, since $R_N > R_1$. This yields a net electric field pointing from the far edge of large electrode towards small electrode during positive AC cycle (Fig. 4(c)). The diffusive positive ions are then dragged from the larger to the smaller electrode. When the cycle reverses, the direction of the field reverses, as well as the sign of the ions. This results in a uni-directional force exerting on the ions in the diffusion layer during all cycles creating a net fluid flow (Fig. 4(d)).

The velocity of ion (v_{ion}) in the diffusion layer can be evaluated from the tangential electric field ($E_t = \Delta V/\Delta L =$

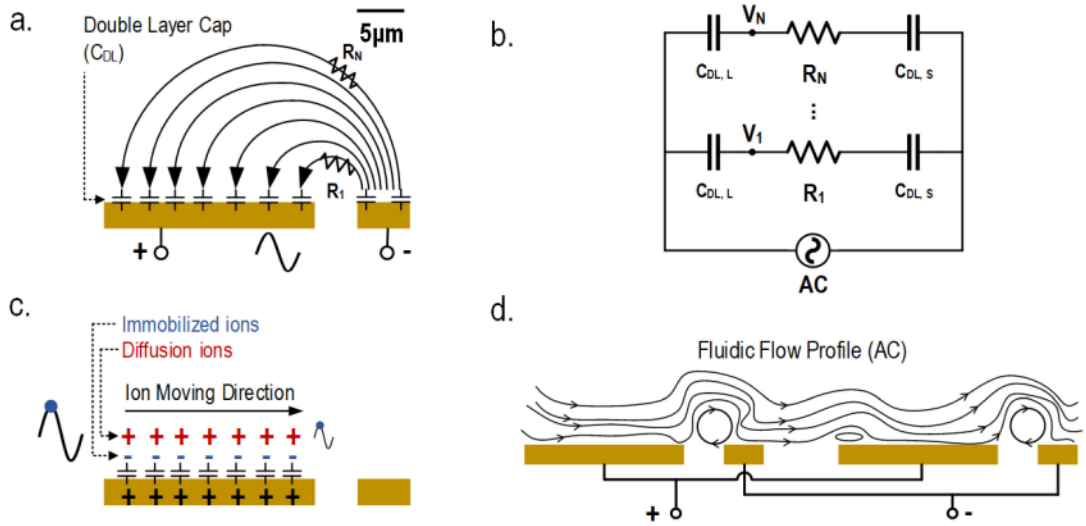

Fig. 4. Operating principle of the induced-charge AC electro-osmosis. (a) Current paths between the asymmetric electrodes through double-layer capacitor (C_{DL}) and bulk fluid resistances (R_1 to R_N). (b) Equivalent circuit model between the asymmetric electrodes under AC excitation. The top-plate voltage of double-layer capacitor for the larger electrode are denoted as V_N and V_1, located at far left and far right respectively. (c) Ionic motion in diffusion layer on the larger electrode during the positive cycle of AC excitation, showing that the net ionic motion points from the larger to smaller electrode irrespective of the AC cycle. (d) Illustration of AC electro-osmosis demonstrating the uni-directional flow can be generated through asymmetric electrode designs and AC excitation voltages with local vortexes on the edge of electrodes.

$(V_{N+1} - V_N)/\Delta L)$ (where ΔL is the separation distance between the two resistors R_N and R_{N+1}) as

$$v_{ion} = \mu E_t = C\frac{\epsilon\zeta}{\eta} \times \frac{\Delta V}{\Delta L} \tag{2}$$

where μ is the ionic mobility, ϵ is the dielectric constant of the fluid, η is the fluid's dynamic viscosity, ζ is the zeta potential at the double-layer (Fig. 3), and C is a constant of value $2/3$ for low ionic concentration [25]. In addition, zeta potential (ζ) represents the potential at the top plate of C_{DL} (Fig. 4(b)), which results in $v_{ion} \propto V_{AC}^2$.

Given the nature of the electrolyte and ionic concentration, the design objective behind choosing the width and gap for the AC osmosis electrodes becomes clear: maximize conversion of electrical energy to kinetic energy of the fluid. This can be achieved by maximizing ΔV at the center frequency ω_0, as shown in (1).

Furthermore, the pumping velocity can be further optimized through increasing electrode height. Prior works demonstrated that by increasing the electrode height, one can generate a local vortex below the main bulk fluid flow, without impinging the flow speed. Therefore the fluid driving velocity can be significantly improved compare to planar electrode designs [33]–[36].

D. Cell Electronic Focusing, Sensing and Separation

Precise control of the cell flow is critical for high sensitivity cytometry. In prior works, hydrodynamic force has been mostly deployed to allow focusing of cell motion within a narrow streamline flow, thereby, enhancing the overall specificity and sensitivity [37], [38]. This requires additional pneumatic-based microfluidic pumps.

An alternative way of manipulating cells in the microfluidic system is through dielectrophoresis (DEP) [39]–[48]. DEP relies on creating a net force on a suspended polarizable particle (such as cells) in a non-uniform electric field.

With the ability to precisely engineer the optimal fields with an array of electrodes controlled by custom CMOS circuits, we can eliminate the need for any hydrodynamic focusing, and replace it with electronic focussing, cell manipulation, and sensing. This is critical to reduce measurement variations due to cell positions. The force exerting on a dielectric particle in a non-uniform field can be evaluated as

$$F_{DEP} = <(P \cdot \nabla)E> = \frac{3\pi}{2}\epsilon_m V \cdot Re(f_{cm})\nabla|E_{rms}|^2 \tag{3}$$

where $P = pV$ is the induced dipole under an external electric field, V is the volume of the particle, E_{rms} is the root-mean-square (RMS) intensity of the electrical field, and f_{cm} is the Clausius-Mossotti factor which quantifies the dipole moment of the particle relative to the solution medium. This factor can be quantified as follows

$$f_{cm} = \frac{\epsilon_p - \epsilon_m}{\epsilon_p + 2\epsilon_m} \tag{4}$$

where ϵ_p and ϵ_m represents the complex permittivity of the particle and the fluid medium. Therefore, with an array of electrodes with independent driving capability, one can engineer the nature of the electric fields within the channel, creating precise positioning of the cells allowing high precision cytometry and subsequent separation capabilities (Fig. 5(b)).

Given that both ϵ_p and ϵ_m depend on frequency, the direction of the DEP forces can change depending on the frequency of operation, offering another degree of freedom to manipulate cells. For example, when red blood cell (RBC) is present in isotonic buffer of 8.5% sucrose + 0.3% dextrose

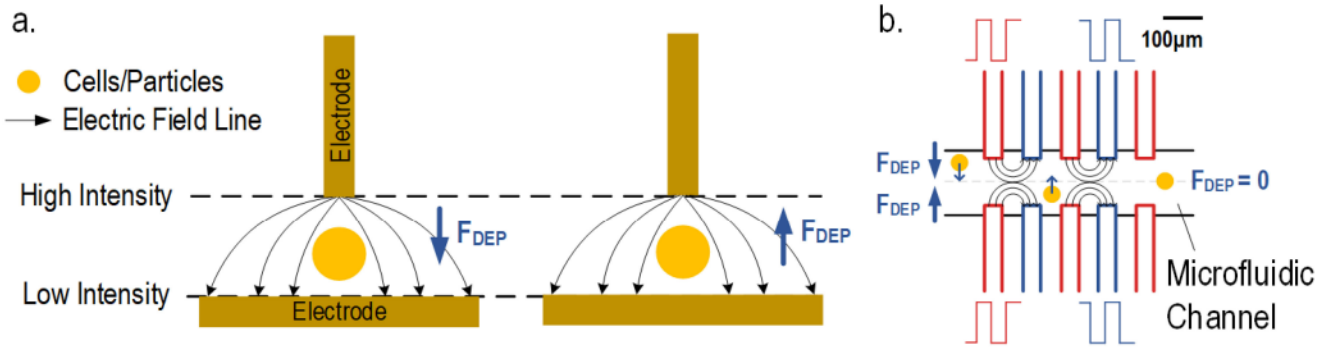

Fig. 5. Cell manipulation through dynamic electric field engineering with an array of electrodes. (a) Dielectrophoretic (DEP) force exerting on the beads/cells, with negative DEP (nDEP) force direction defined as pointing towards low electric field intensity and vice versa for positive DEP (pDEP). (b) An illustration of DEP combined with microfluidic channel. Red and blue electrodes generating electric fields in the channel. In the case of nDEP, beads/cells will experience a net force pointing towards the center line, where $\nabla E = 0$.

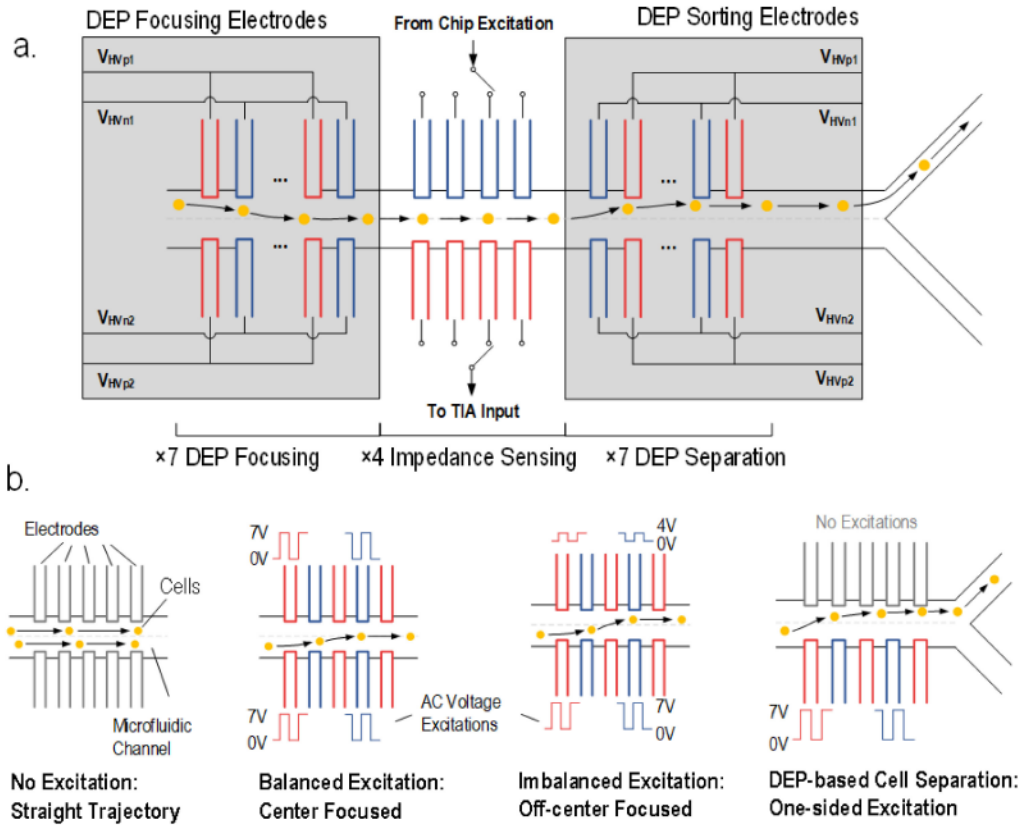

Fig. 6. Electric field synthesis for cell manipulation. (a) System of electrodes containing cell focusing (7 pairs), sensing (4 pairs) and separation (7 pairs) functionalities. The figure shows electronic cell focusing for robust measurements, and subsequent separation. (b) Illustration of four possible DEP operating conditions: excitation signals are turned off, balanced excitation signals are fed into the two sides of electrodes, imbalanced signal is activated, and only one side of the electrodes are activated.

($\approx 60\text{mS/m}^{-1}$), the inversion of DEP force occurs at around 1 MHz (Fig. 7) [39]. At low frequencies, $Re(f_{cm}) < 0$, and negative DEP (nDEP) forces exert on the cell pushing it towards the direction of lower electric field intensity (Fig. 5(a)). Beyond the first crossing point, $Re(f_{CM}) > 0$, and the force reverses its direction. At very high frequencies close to GHz, $Re(f_{CM})$ turns negative again, but the force magnitude is much smaller compare to the first nDEP region. In this particular work, a stronger nDEP operating in the range of hundreds of kHz is selected. Stronger nDEP is chosen for cells to experience net force pointing towards the center of channel with the highest focusing accuracy under equal excitation amplitudes (2 μm error), as shown in later measurement results. High accuracy of focusing is necessary to ensure consistent impedance

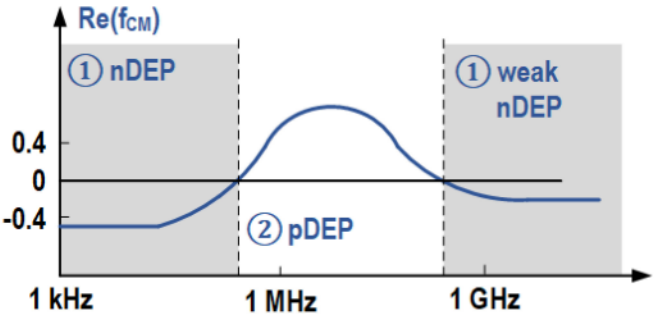

Fig. 7. Variation of f_{CM} as a function of electric field frequency for red blood cells. Fluid medium conductivity and dielectric constant is set to 60 mS m^{-1} and 78 ϵ_0. In addition, the conductivity and dielectric properties are set at 310 mS m^{-1} and 59 ϵ_0 respectively [39].

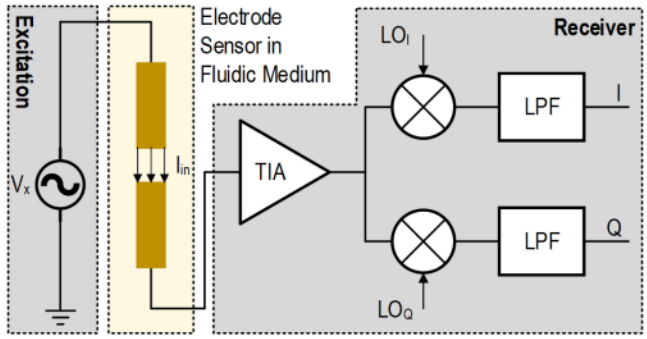

Fig. 8. Impedance spectroscopy sensing based on direct conversion architecture. Core components required include voltage excitation, impedance sensing electrodes, TIA, down-conversion mixer and low-pass filters.

measurements, which will be demonstrated in later sections of this paper.

For DEP to operate effectively, the required electric field intensity is reported to be on the order of 10^5 – 10^6 V/m [49], [50]. This indicates that under 5 V of voltage excitation, the separation of the DEP electrode within the microfluidic channel is around 50 μm.

With the aforementioned functionalities, we realize a system of electrodes capable of performing cytometry, cell actuation and AC osmosis driver on a single glass substrate [51]–[53]. As shown in Fig. 6(a), a series of gold electrodes are aligned in the microfluidic channel. The first seven pairs of electrodes are dedicated to cell focusing, where the electric field within the channel can be synthesized on the fly by controlling the difference of the AC voltage magnitudes on either side of the channel. The frequency, in the work, is chosen below 500 kHz such that the cells only experience strong nDEP force.

As shown in Fig. 6(b), when the electrodes are not excited, the cells will pass along the channel with randomly distributed lateral positions. In the case of balanced voltage excitations, the gradient of the electric field will be minimized in the center of the channel. Therefore, the cells will be center-focused. In the case of imbalanced excitation, the minimum gradient will be pushed towards the side with smaller voltage excitation, resulting in an imbalanced cell focusing [53]. In an extreme case, where only one side of the electrodes are activated, cells will be completely pushed towards one side of the channel. In this case, the configuration can be used to separate the cells into different diverging channels, indicated by the last seven pairs of electrodes.

In between the cell focusing and separation electrodes, are four pairs of impedance sensing electrodes that are able to capture cell flow in the microfluidic channel in real-time. The top four electrodes are designated for voltage excitation, where the bottom four are directly connected to the receiver inputs.

The DEP and impedance sensing electrodes are located on the two sides of the microfluidic channel with a lateral separation of 50 μm to realize a stream of cell processing functionality in the following order: cell focusing, sensing and cell separation. Specifically, a lateral separation of 50 μm is chosen to ensure cells that enter the center portion of the channel. Both DEP and impedance sensing electrodes are designed with a width of 40 μm and horizontal pitch of 70 μm, to ensure the sensors are able to capture large cells/beads beyond 10 μm. Although prior works have demonstrated that both DEP and impedance sensing performance can be improved by elevating the electrode in the third dimension, height, so that the effect of non-uniform electric field distribution can be eliminated [43], [51], [53], we choose to design electrodes in 2-D as a proof of concept for this work (Fig. 9(c)). The electrode dimensions for AC osmosis are shown in Fig. 20(a) on the same glass substrate.

E. Impedance Spectroscopy Sensing

Built on top of the AC electro-osmosis bulk fluid driver and DEP cell actuation, is a 16-array impedance spectroscopy receiver based on a direct conversion architecture. The purpose of the impedance spectroscopy sensing is to provide the impedance measurements in real-time at the electrode-electrolyte interface [54]. This sensing modality is employed for cytometry sensing, and for label-free protein bioassay in this multi-modal biosensing platform. As shown in Fig. 8, the impedance spectroscopy sensing system constitutes a low-noise transceiver system, including voltage excitation driver, transimpedance amplifier (TIA), in-phase (I) and quadrature (Q) mixer as well as low-pass filter (LPF).

The voltage source, V_x, shown in Fig. 8, excites the sample at a frequency that is optimized for extracting the highest response from the sample. The changing event (such as protein-protein binding or cell passing) creates a transient change in dielectric constant locally, resulting in a deviation of input current signal ($I_{in} = A_I \cdot \sin(\omega t + \phi)$) amplitude ($A_I$) and phase ($\phi$). The TIA converts the input current to voltage with a transimpedance gain of A, and detects the amplitude and phase change to infer about the biosensing event. Prior works have shown that the sensitivity for immunoassays can be maximized by operating frequencies around 500 kHz-1 MHz [55], [56]. In this work, we primarily focus on probing both cytometry and immunoassays around f_0=500 kHz.

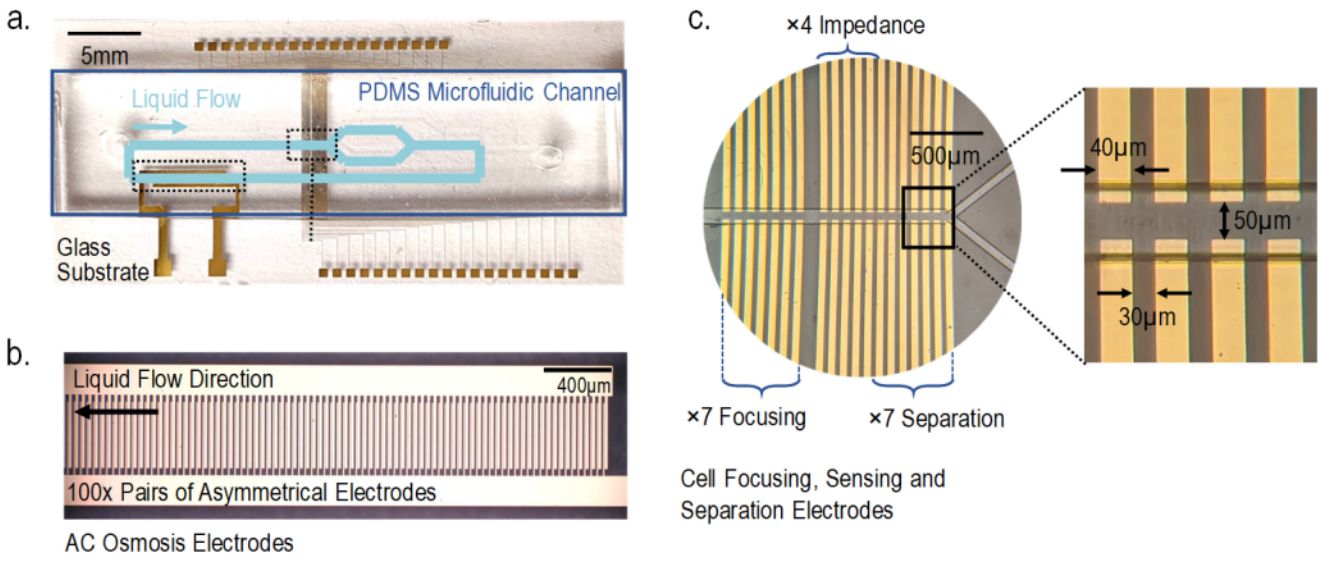

Fig. 9. Fabricated fluidic system and electrodes. (a) Fabricated gold electrodes on glass substrate, containing AC osmosis bulk fluid driving and system of DEP actuation and impedance sensing electrodes. Microfluidic channel made of PDMS is permanently bonded on top of glass substrate. (b) A zoomed view of 100 pairs of asymmetric AC osmosis electrodes. (c) A zoomed view of the system electrodes, containing cell focusing, sensing and separation electrodes.

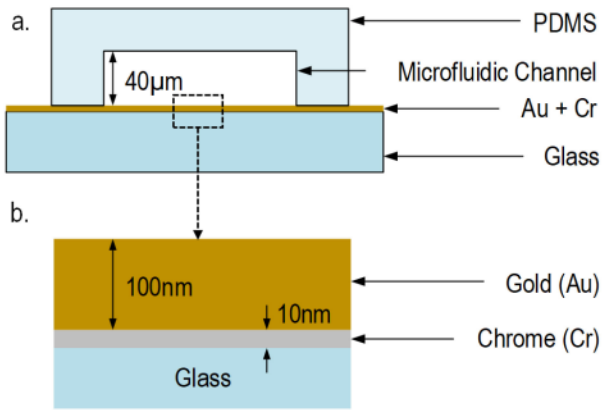

Fig. 10. Microfluidic assembly. (a) A side view of the fully assembled electrode-channel interface. (b) A zoomed view of the electrode-glass interface with gold electrodes deposited on top of chrome as adhesive layer.

III. Microfluidic Device Fabrication and Assembly

The microfluidic flow assembly is shown in Fig. 9. The sample through the inlet is driven by a set of AC-osmotic electrodes controlled by the chip. The sample then passes through the described set of electrodes for cell focusing, sensing and separation. The processed fluid can be further investigated for protein sensing, as described later.

A. Electrode Fabrication

In this work, borosilicate float glass is used as substrate. The electrode pattern is fabricated through standard photolithography procedure. First, a 10 nm layer of Chrome (Cr) is deposited as an adhesive layer, followed by a 100 nm of gold (Au) layer deposition. Au is chosen as the interface between the electrode-electrolyte interface, to take advantage of its inert chemical nature with ionic liquid. The deposition is conducted with an e-beam evaporator (Angstrom Engineering Inc, Canada). Next, the metal layer was removed with the photoresist, and the electrodes were formed by a lift-off process. The resulting glass-metal interface is demonstrated in Fig. 10.

B. Microfluidic Channel Fabrication and Assembly

The PDMS microfluidic channels are fabricated through soft photolithography. Initially, an SU-8 2025 layer was spin-coated at 3000 rpm on a silicon wafer and soft-baked at 65 °C for 1 min and 95 °C for 6 min. The wafer is then exposed to UV and is post-exposure baked at 95 °C for 6 min. After that, the wafer was developed using SU-8 developer (Microchem, Newton, MA), followed by necessary washes with isopropanol and drying. The mold wafer was then used for PDMS casting. with curing temperature set to 80 °C for one hour. Finally, the PDMS was peeled off and punched with 1.5 mm-diameter holes for fluid inlets and outlets.

The microfluidic channel has a height of 40 μm, and is aligned over the gold electrode device using a home-made aligner that consist of 3-axis micromanipulators and microscope. Finally, the PDMS channels were covalently bonded to the glass substrate using UV/O_3 cleaner (BioForce Nanoscience, USA) for 20 min. The device is then incubated at 95 °C for 20 min on a hot plate to increase the bonding strength. The UV/O_3 and heating treatment can allow tight covalent bonding between PDMS and glass substrate to prevent fluid leakage. Finally, the complete channel-electrode interface is illustrated in Fig. 10(a).

IV. Circuits and System Implementation

This section will illustrate the on-chip architecture for controlling AC-osmotic flow, cell flow, and sensing with integrated impedance spectroscopy. The chip is designed and fabricated in

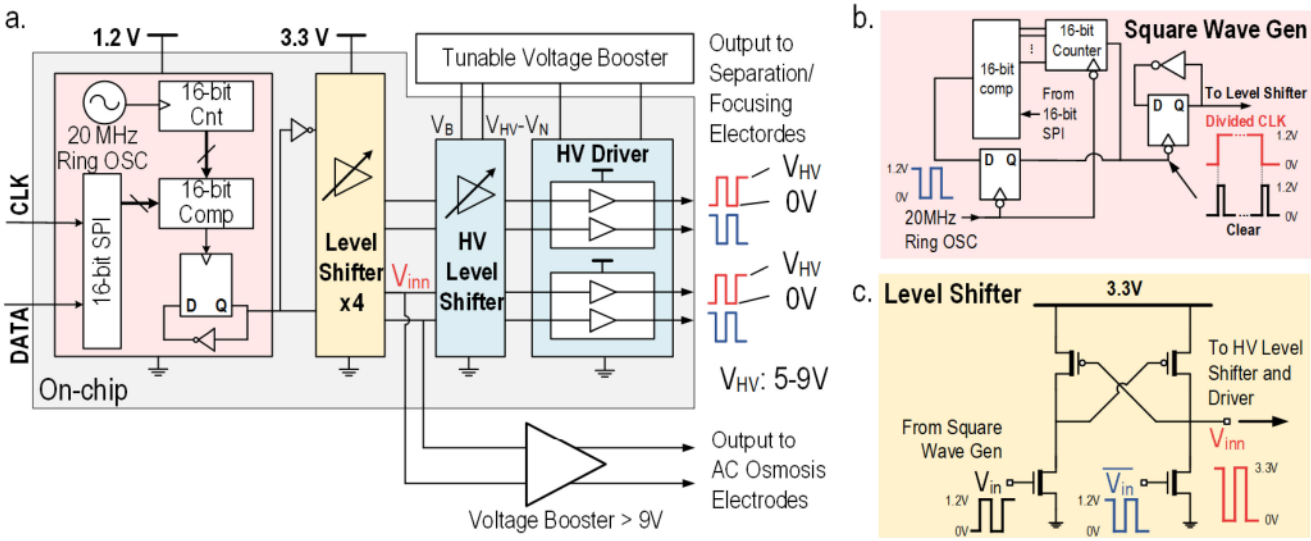

Fig. 11. AC-osmosis and DEP driver architecture and circuits. (a) Architecture of the DEP and AC osmosis driving chip, capable of generating 5-9 V of driving signals at HV driver outputs for DEP. (b) On-chip programmable square wave generator. (c) 3.3 V level shifter.

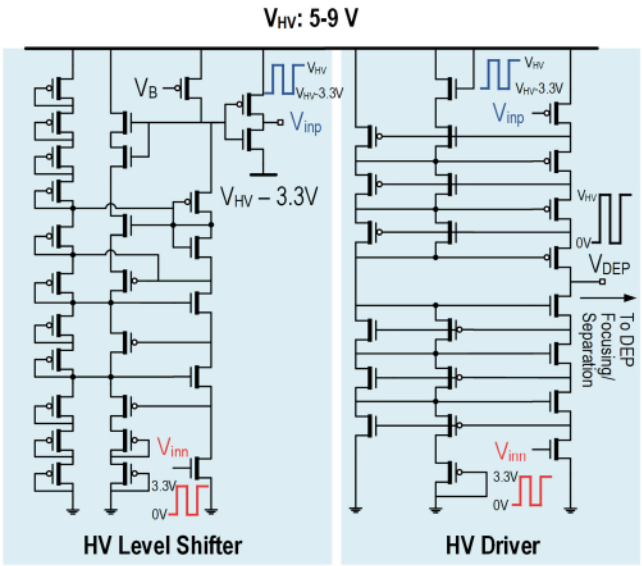

Fig. 12. High-voltage (HV) level shifter and driver, using stacked topology capable of generating 5-9 V of driving signals for DEP.

TSMC 65-nm LP bulk CMOS process. This particular process is chosen to optimize the performance at low power operation for POC applications.

A. AC-Osmosis and DEP Driver Architecture

To provide a driving signal for both the AC electro-osmosis and DEP electrodes, the system includes a programmable signal generator. We employ on-chip high voltage drivers for the DEP system (>5 Vpp). We further boost the signal with off-chip drivers for swings higher than 10 Vpp for AC osmosis. While the boosting was achieved off-chip for AC-osmosis in this proof-of-concept chip, this can be easily integrated in a longer node CMOS process with a higher breakdown voltage limits.

Fig. 11 shows the circuit architecture for the high-voltage square wave generator. It consists of three major components: programmable square wave generator operating at 1.2 V with SPI interface, a 3.3 V digital level shifter, and high-voltage level shifter and driver for DEP electrodes.

1) Programmable Square Wave Function Generator: The core of the square wave function generator consists of a 20MHz three-stage ring oscillator and a 16-bit synchronous counter. The 16-bit counter can be periodically reset through the comparators, where the resetting time can be digitally controlled through a SPI interface (Fig. 11(b)). With this approach, the square wave generator block is capable of providing driving frequencies from 300 Hz to 10 MHz that is sufficient to cover the operations of both AC osmosis and DEP.

2) High-Voltage Level Shifter and Driver: The output of the 1.2 V square wave is level shifted to a 3.3 V reference (realized with thick-oxide devices), as shown in Fig. 11(c). This signal is then sent to the on-chip high-voltage (HV) level shifter and driver to generate the DEP signal (Fig. 12) or sent off chip to generate the AC electro-osmotic drive signals.

The HV level shifter, in particular, uses a stacked topology with thick oxide transistors and with self-biasing circuitry to simplify the overall design and complexity (Fig. 12) [57]. We ensure that the node voltages are kept within the safe limits, and the maximum swing is set by the p-n junction breakdown voltage (9 V) of the source/drain and substrate region. As shown in Fig. 12, HV level shifter converts a 3.3 V square wave (V_{inn}) to level-shifted 3.3 V square wave (V_{inp}) for the HV driver. The circuit is realized through three vertical branches of stacked transistors. V_{HV} is set through a boost converter, and can be tuned from 5-9V to cover a sufficient supply voltage for DEP electrodes. The biasing current, controlled through V_B, is set such that when V_{inn} is low, the top PMOS has the capability to

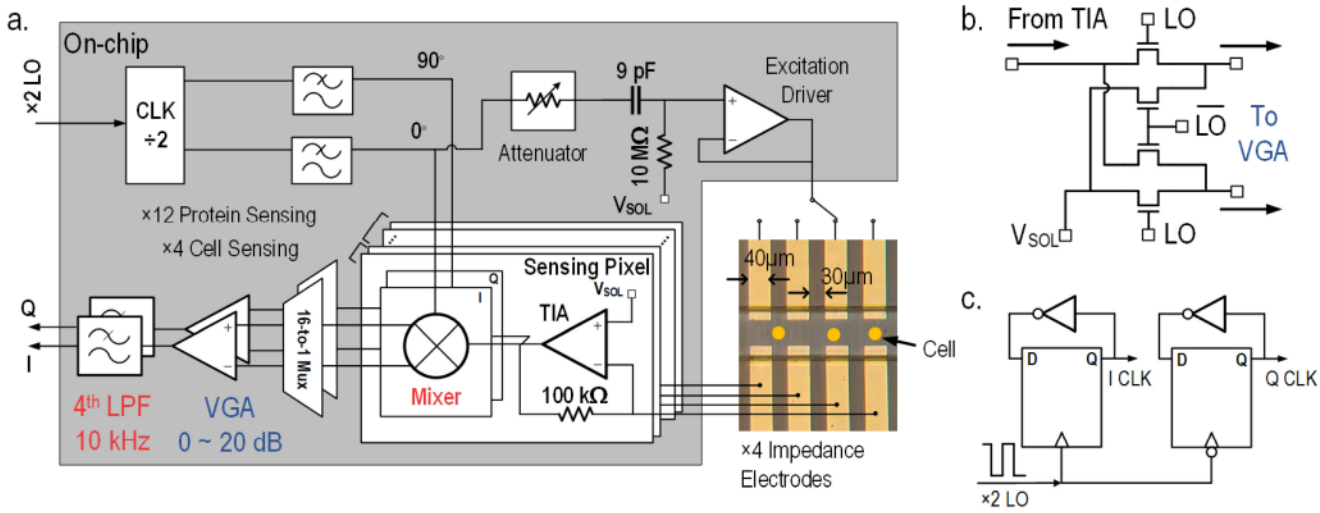

Fig. 13. Receiver architecture for impedance spectroscopy. (a) 16-element architecture (4 dedicated to cell sensing and 12 to protein sensing) containing the excitation and receiver paths. (b) Passive double-balanced mixer. (c) On-chip I and Q clock generator from a single ×2 LO frequency.

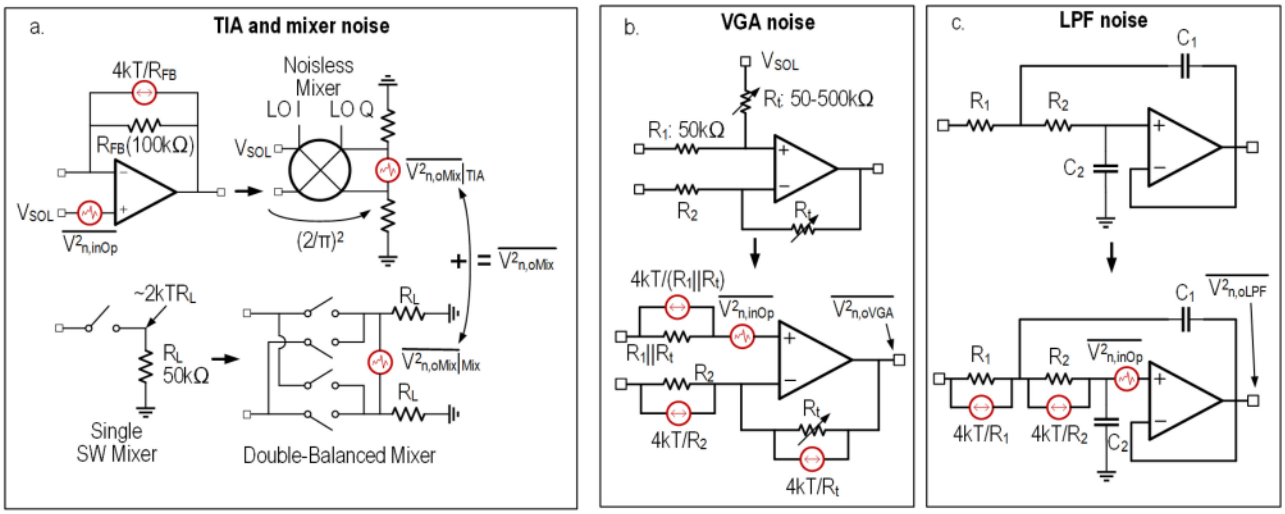

Fig. 14. Noise analysis in the receiver path. (a) TIA and mixer noise. (b) VGA noise. (c) LPF noise.

pull up the gate voltage of the inverter stage. Therefore V_{inp} can be pulled down to $V_{HV} - 3.3V$. Next, both V_{inp} and V_{inn} are fed into the HV driving stage together, which also consists of three vertical branches of stacked transistors. The first two vertical branches of stacked transistors on the left of the HV driver are necessary to provide proper biasing voltages for the stacked transistors at the output (V_{DEP}). In summary, the output of the HV driver is capable of generating square wave driving signal between 5-9V. Two HV drivers generate a differential signal pair that drives the DEP focusing and separation electrodes, that is sufficient to cover the minimum electric field intensity (10^5 V/m) required for DEP electrodes with 50 μm of separation. Together, the HV level shifter and the output driver circuit consume roughly 30μA of current from 7 V of supply voltage without considering the dynamic output loading current.

B. Impedance Spectroscopy Receiver Architecture

The purpose of the direct conversion receiver, as aforementioned, is to provide real-time impedance sensing for the cytometry in the microfluidic channel and for protein sensing (Fig. 13).

1) Excitation Path: The excitation signal is generated internally through the divide-by-2 I/Q clock generator (Fig. 13(c)). It is implemented through two flip-flops capable of providing both the in-phase and quadrature-phase waveforms. The in-phase signal then has the option to be low-pass filtered to remove the higher order harmonics from the square wave, and then fed to a programmable attenuator (realized through resistor divider). The signal is then high-pass filtered through combination of on-chip MOM capacitor (9 pF) and resistor (10 MΩ poly resistor) to pin the output DC voltage to V_{SOL} (Fig. 13(a)). The design of the excitation driver is based on a standard two-stage op-amp with

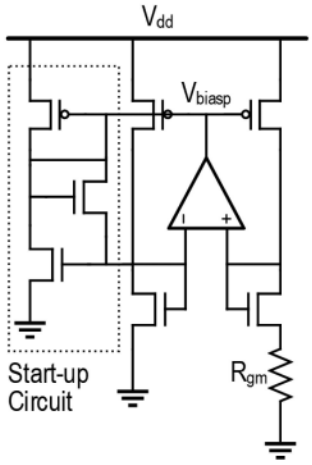

Fig. 15. Constant-gm biasing with start-up circuit to prevent V_{bias} been latched to V_{dd}.

capacitive miller compensation. The op-amp driver is designed with bandwidth of 10 MHz capable of penetrating the double-layer capacitance (C_{DL}) at the electrode-electrolyte interface.

2) Trans-Impedance Amplifier (TIA): We employ an op-amp based TIA with a R_{FB} of 100 kΩ in feedback to achieve a bandwidth of 2 MHz. The op-amp topology employed in the TIA is similar to the driver op-amp in the excitation path. However, in this design, the length of the input differential pair is significantly increased to 1 μm to minimize the $1/f$ noise. Since the subsequent passive mixer translates the noise spectrum, the output voltage noise of the receiver path has a significant contribution from the VGA and LPF due to the low signal bandwidth (10 kHz) and the presence of 1/f noise from later stages.

In addition, four pairs of TIA input channels are deployed for impedance cytometry sensing. This is primarily to address the issue with any false positive or missing detection caused by single channel activation. This can be reduced by sweeping through the pixels in sequential order. In addition, slight variations in pixel gains, due to TIA and mixer mismatches, can be calibrated.

3) Passive Mixer, Differential-to-Single-Ended VGA and LPF: We use a double-balanced passive mixer to minimize power consumption, LO feed-through, and maximize the conversion gain (Fig. 13(b)). To further increase the sensitivity of the receiver, we use additional programmable VGA with a digitally tunable gain ranging from 0-20 dB (Fig. 14(b)). After the programmable VGA, we employ a LPF to filter higher order harmonics. The LPF is designed with a 4-th order Butterworth response by cascading two second order Sallen-Key LPF in series [58] (Fig. 14(c)). Together, the overall LPF is capable of achieving a 10 kHz filtering bandwidth with 80 dB/dec roll-off beyond the 10 kHz cutoff frequency.

To bias all the analog components, the chip deploys a constant-gm self-biasing circuit in order to minimize the usage of external biasing pads. As shown in Fig. 15, due to the short channel nature of 65-nm LP process, the constant-gm biasing core is designed with additional differential-to-single-ended amplifier to operate across a wide range of supply voltages. In addition, a start-up circuit is designed to provide a discharging path to avoid V_{biasp} being latched to V_{dd}. With this design approach, the constant-gm self-biasing circuit is able to achieve a consistent 20 μA across a wide range of supply voltages between 1.2 and 2.5V.

C. System Noise Analysis

The noise of the system is primarily contributed by a combination of the input TIA, mixers, VGA and the low-pass filters, as shown in Fig. 14. A major design challenge of the impedance spectroscopy receiver is that the spectrum of the desired signals (such as for cytometry) is located below 10 kHz. This is primarily determined by the dynamics of the biosensing interface such as the flow velocity of the cells that move across the electrodes array. As an example, for an AC osmotic flow rate of 100 μm/s (as we will see in the measurement section), the time taken for a cell to pass through one sensing electrode of width 40 μm is ∼0.25 s. To capture this dynamic with high sample rate (to identify and classify different cells, if needed) we keep the integration time below 0.1 ms, or in effect, the integration is set around 10 kHz by the LPF. Therefore, the 1/f noise of the circuitry after the frequency translation of the mixer becomes critical.

1) TIA and Mixer Noise: The output noise of the TIA around the frequency of analysis ($f_0 \approx 500$ kHz) gets translated down to the signal frequency at baseband after mixing. As show in Fig. 14(a), the output voltage noise spectrum of the TIA can be calculated as

$$\overline{V^2_{n,opTIA}} = 4kTR_{FB} + \overline{V^2_{n,inOp}} \tag{5}$$

where $\overline{V^2_{n,inOp}}$ represents input voltage noise of the op-amp used in the TIA. After frequency translation through the differential passive mixer with an average fundamental frequency voltage gain of $2/\pi$, the receiver output noise spectrum due to TIA alone has a spot noise of $0.18\text{pV}^2/\text{Hz}$. When integrated over the 10 kHz LPF bandwidth, the TIA noise contribution at the receiver output yields around 42 μV of r.m.s. noise voltage.

In addition, assuming fast switching with 50% duty cycle in the double-balanced passive mixer, the output noise spectrum contributed by the mixer itself, can be approximated as $8kTR_L$, where R_L is the equivalent output loading resistance of mixer [59]. Combining TIA noise, the net spot noise at the output of the receiver, due to the TIA and the mixer circuits can be evaluated to be $0.32\text{pV}^2/\text{Hz}$. Within the LPF bandwidth of 10 kHz, the total noise contribution due to TIA and mixer combined can be calculated to be ≈ 57 μV of r.m.s. noise voltage.

2) Programmable VGA and LPF Noise: As mentioned before, the

$$\overline{V^2_{n,oVGA}} = A^2_{VGA}(4kT(R_1||R_t) + 4kT(R_2||R_t) + \overline{V^2_{n,inOp}}) \tag{6}$$

$1/f$ noise portion in VGA is critical in the total noise contributions. Shown in Fig. 14(b) are the noise contributors. The noise voltage at the input of the VGA due to $R_1||R_t$ and $R_2||R_t$ can be evaluated as $4kT(R_1||R_t + R_2||R_t)$. The total

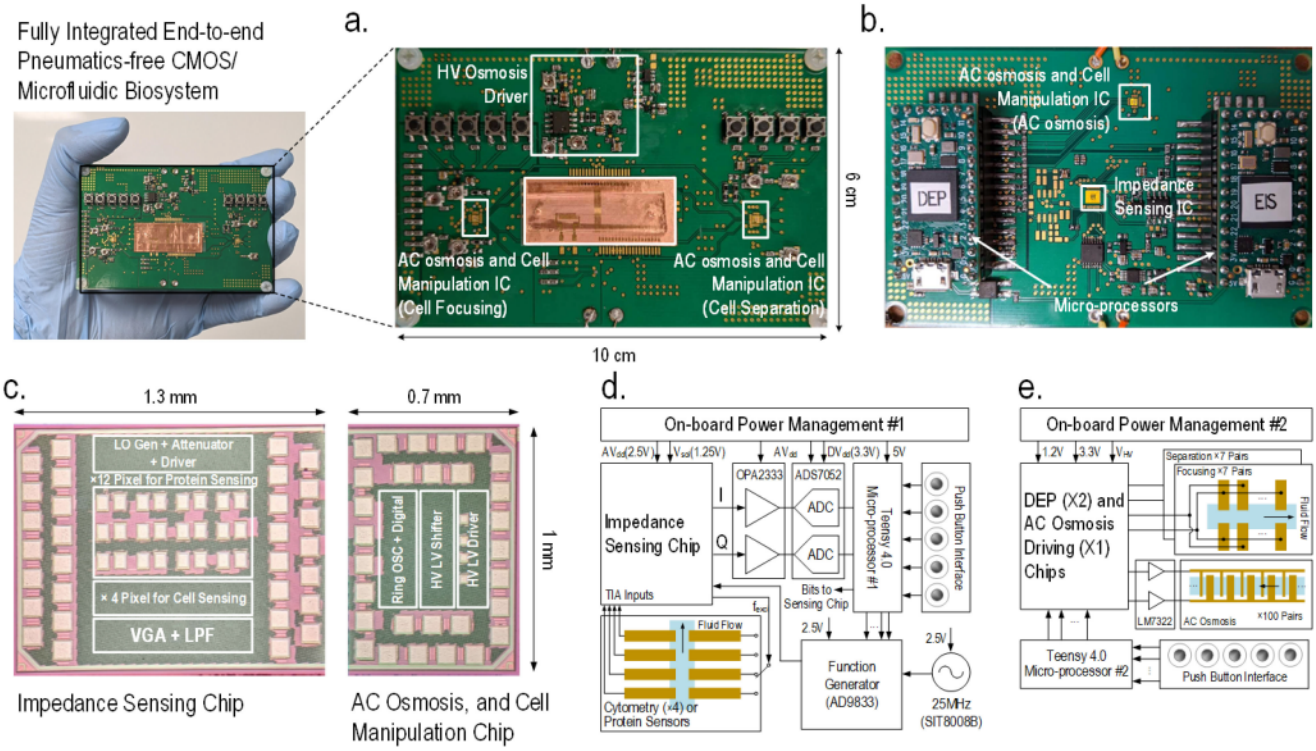

Fig. 16. CMOS-based pneumatic-free microfluidics and biosensing platform. (a) Front view of the system showing the fluidic interface and the AC-osmotic and DEP controlling chip. (b) Back view of system showing the impedance sensing chip. (c) Die photo of the CMOS chips for impedance sensing, AC osmosis and DEP cell actuation. (d) and (e) PCB system schematics for the impedance sensing, and AC osmosis and DEP driving circuitries respectively.

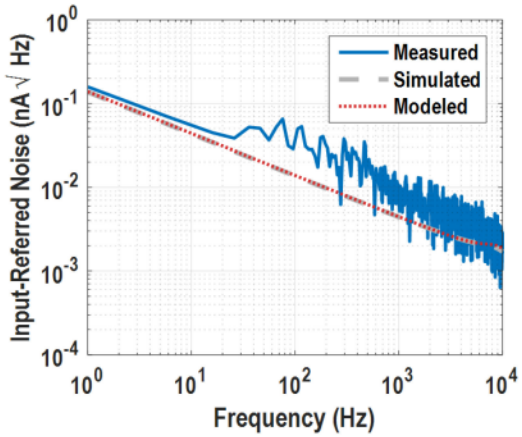

Fig. 17. Measured input-referred current noise in comparison with simulated (Cadence) and modeled results. The modeled results are derived from hand calculation from each receiver stage and referred to the input noise current.

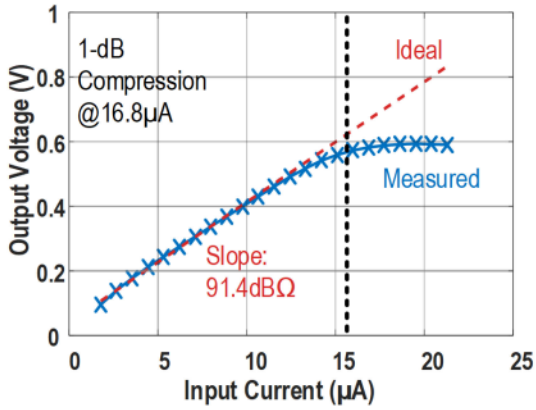

Fig. 18. Linearity and gain measurements showing a measured TIA gain of 91.4 dB Ω and 1-dB output compression at 16.8 μA.

$1/f$ and white noise due to the op-amp can be represented as the input-referred noise ($\overline{V^2_{n,inOp}}$). Therefore, the total noise at the output of the programmable VGA ($\overline{V^2_{n,oVGA}}$) due to the contributions in Fig. 14(b) can be represented as where A_{VGA} is the gain of VGA and it is set to 20 dB. The input-referred noise spectrum density of op-amp ($\overline{V^2_{n,inOp}}$) is simulated to be $(0.19\text{nV}^2/\text{Hz})/f + (0.16\text{fV}^2/\text{Hz})$. The receiver output noise spectrum due to VGA, under maximum gain of 20 dB, can be evaluated to contribute a net noise of ≈ 415 μVrms within the 10kHz of LPF bandwidth.The receiver output noise due to the active 4-th order LPF ($\overline{V^2_{n,oLPF}}$) can be evaluated by considering the transfer functions from each noise source within LPF to the output node, as demonstrated in Fig. 14(c). Table I summarizes the small signal transfer function from each noise source to the output of the 2-nd order LPF, and the output noise due to LPF alone is ≈ 117 μVrms.

Analysis of the noise sources show that the dominant noise source in the receiver chain, as predicted, arises from the 1/f

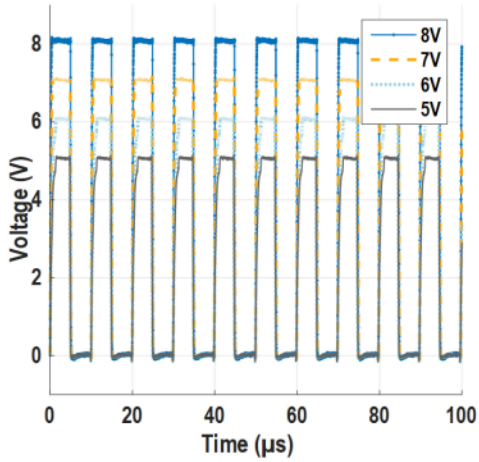

Fig. 19. High-voltage output waveform of the DEP HV driver ranging from 5-8 V of output swing.

TABLE I
TRANSFER FUNCTIONS OF MAJOR NOISE SOURCES IN LPF TO LPF OUTPUT

Noise Sources	$T(s)$
V_{in}	$1/(R_1R_2C_1C_2)/D(s)$
$\overline{I^2_{n,R1}}$	$1/(R_2C_1C_2)/D(s)$
$\overline{I^2_{n,R2}}$	$[s/C_2 + 1/(R_2C_1C_2)]/D(s)$
$\overline{V^2_{n,inOp}}$	$[s^2 + (1/(R_1C_1) + 1/(R_2C_1) + 1/(R_2C_2)s + 1/(R_1R_2C_1C_2)]/D(s)$
	$D(s) = s^2 + [1/(R_1C_1) + 1/(R_2C_1)]s + 1/(R_1R_2C_1C_2)$

noise in the VGA. The signal acquisition path for both cell and protein sensing is co-designed with the electrode and the receiver design, resulting in measured SNR of 10 dB and higher for cell sensing measurements, as shown later in the paper. While these metrics can be further optimized, the achieved sensitivity allow us to demonstrate the principles of multi-modal functionalities of the presented platform.

V. MEASUREMENT RESULTS

In this section, we present the overall packaging, electrical performance, CMOS-driven AC-osmotic flow, cell manipulation, and biosensor measurements.

A. CMOS Packaging and PCB System Implementation

The overall system is shown in Fig. 16. The custom-designed ASIC is fabricated in TSMC 65-nm LP process. The chip photographs are shown in Fig. 16(c). As the figure shows, the DEP/AC osmosis chips are mounted both on the front and back-sides of the PCB, and the impedance sensing chip is mounted at the back (Fig. 16(a)–(b)). All the chip I/Os and the passive microfluidic electrodes are wire-bonded to PCB. In addition, there are also peripheral surface mount circuitries that control, monitor and process the signals into and out from the custom ASIC.

The biosensing platform is powered by two sets of AA batteries. Fig. 16(d)–(e) demonstrate the system schematics that are laid out to minimize cross-talk between the DEP/AC osmosis drivers, and the impedance spectroscopy receivers.

B. Electrical Characterization of Impedance Sensing Chip

To characterize the sensitivity of the receiver, we connect the receiver output to an off-chip low-noise pre-amplifier (Stanford SR560) and subsequently to a spectrum analyzer (R&S FSW) to acquire the output noise voltage spectrum. The measured input-referred current noise is illustrated in Fig. 17. At a bandwidth of 10 Hz, 100 Hz and 1 kHz, the input-referred current noise is measured to be 301, 536 and 812 pA r.m.s. respectively.

To measure the linearity of the receiver, we connect a 10 k Ω resistor between the excitation path and the TIA input. The VGA is set to unity gain for maximum linearity. As shown in Fig. 18, the 1-dB compression is measured for an input current of 16.8 μ A. Combined with the input referred noise of 301 pA r.m.s. at a bandwidth of 10 Hz, the impedance sensing system is capable of achieving a total dynamic range of 95 dB. In summary, the input-referred noise and linearity performance is compared against other state-of-the-art CMOS impedance biosensors (Table II), providing sufficient sensing capability for both cell cytometry and protein assay.

C. DEP and AC Osmosis Driving Signals

To test the high voltage driving capabilities across frequency, we send a 16-bit code to the chip that sets the output frequency. Fig. 19 demonstrates a measured driving waveform at the output of the HV driver, ranging from a supply voltage of 5-8 V, demonstrating sufficient electric field intensity ($> 10^5 \mathrm{V/m}$) for the DEP focusing and separation electrodes.

Since the entire device is powered on battery, power consumption of the DEP and AC osmosis driving circuit is of concern for this application. Specifically, at 0.001× PBS concentration, the equivalent resistance between the 7 pairs of DEP and 100 pairs of AC osmosis electrodes are on the order of tens of MΩ and a few MΩ respectively. With driving voltages on the order of 5-18 Volts, the power consumption due to the driver is quite insignificant given the power density of a typical AA battery are on the order of 1-3 Wh.

D. AC Electro-Osmotic Flow Characterization

To characterize the AC-osmotic fluid flow, we drive the electrodes and measure the fluid flow on the other side of the microfluidic channel by observing the bead velocity and to eliminate the effect of DEP on the beads (Fig. 20) [29]. As shown in Fig. 21(b), two floating electrodes, each with a width of 100 and 200 μm are fabricated far away from the AC osmosis electrodes to accurately measure the bulk fluid velocity. As described in the previous section, the osmotic flow is dependent on the electrode width, separation and fluid ionic concentration. In this work, 0.001× PBS concentration is injected in the microfluidic channel to maximize the double-layer diffusion length. To accurately measure the fluid velocity, 1 μm of polystyrene beads

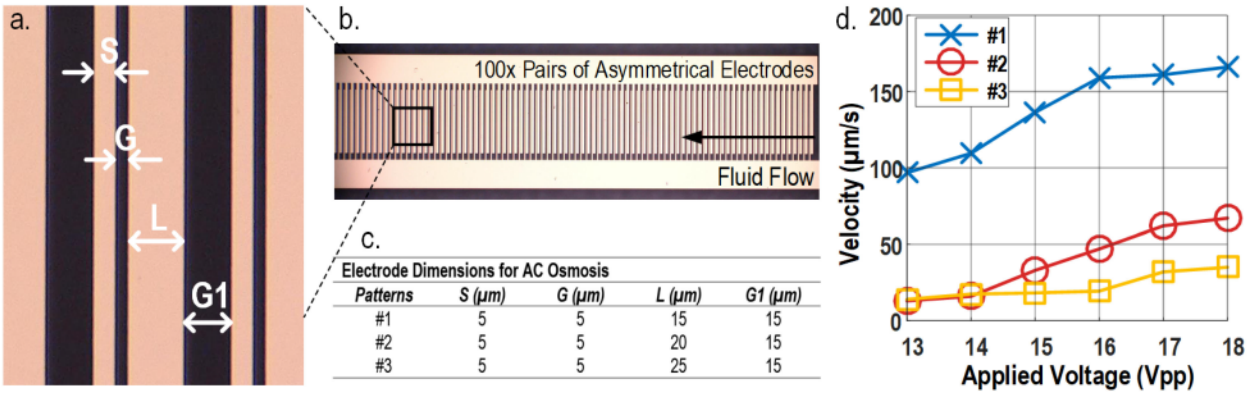

Fig. 20. AC-osmotic flow measurements. (a) A zoomed view of the AC osmosis electrode geometry in (b). (c) Dimensions for different electrode geometries. (d) AC osmosis velocity characterization among three different electrode patterns in c, demonstrating a top velocity of 160 μm/s achieved with 18 Vpp excitation for pattern #1.

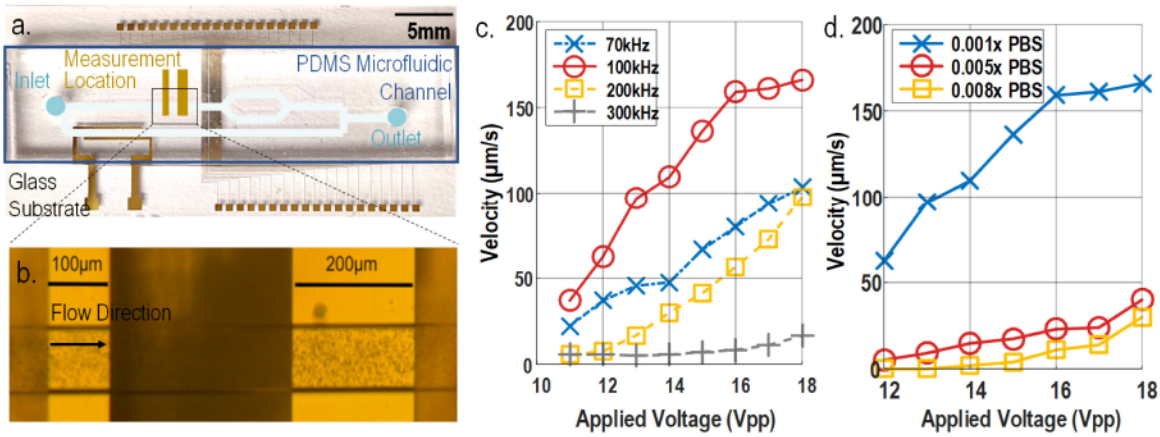

Fig. 21. AC-osmotic flow measurements. (a) Measurement location for the AC osmosis showing relative to entire glass substrate. (b) A zoomed view of the two floating electrodes with 1 μm beads flowing on top of them. (c) and (d) Bulk fluid velocity characterizations for pattern #1 under different excitation frequencies and PBS concentrations.

is mixed with the PBS solution. The small bead size is chosen to minimize the fluid drag effect while remaining observable under a microscope.

In summary, the fluid driving capability is measured in following order. First, the 1 μm polystyrene beads (Sigma-Alrich LB11) is mixed with 0.001$\times$ PBS (diluted from 1$\times$ PBS solution). Then, the fluid mixture is injected in the microfluidic channel. Next, a 100 kHz driving frequency is turned on from the CMOS chip with varying amplitude. Finally, the fluid velocity is determined by measuring the time that the 1 μm beads takes to travel across 100 and 200 μm electrodes respectively.

As explained in Section II, ionic concentration is an important factor that determines bulk fluid velocity. In particular, low ionic concentration results in a longer diffusion length. On the other hand, it also creates a larger equivalent liquid resistance (R_1 to R_N in Fig. 4). As shown in (1), the center frequency (ω_o) is proportional to $1/(C_{eq}\sqrt{R_1 R_N})$. Therefore, by decreasing the ionic concentration, the center frequency (ω_o) decreases as well. One risk of operating at lower frequencies in the range of tens of kHz, is the possibility of electrolysis, bubble formation and eventual electrode damage. This phenomenon has been reported in prior works [29]. Therefore, low frequency operation is generally avoided on this platform.

A balance between the ionic concentration, frequency, and the electrode dimension is experimentally optimized and summarized in Figs. 20 and 21. In summary, pattern #1 with a large electrode width of 15 μm appear to have the best fluid velocity with top speed reaching nearly 160 μm/s at 100 kHz. This translates into roughly 0.1 μL/min of fluid volume processing.

The authors would like to emphasize again that the proposed electrode geometry with 160 μm/s of velocity, does not set the upper limit of what AC electro-osmosis can achieve in general. Optimized electrode gemotery can allow more efficient vortex generation and fluid drag with 1% atm pressure [35]. Such high pumping pressure can even be used to drive high ionic buffer fluid (>100 mM) through slipping velocity, allowing indirect pumping of sampled bio-fluid to achieve complex bioassay, such as DNA hybridization [35] and protein-protein interaction straight from human serum sample [23]. This solves the issue where high ionic bio-sample fluid cannot be manipulated directly through AC electro-osmosis, opening up a range of applications in biosensing. In this proof-of-concept work, we

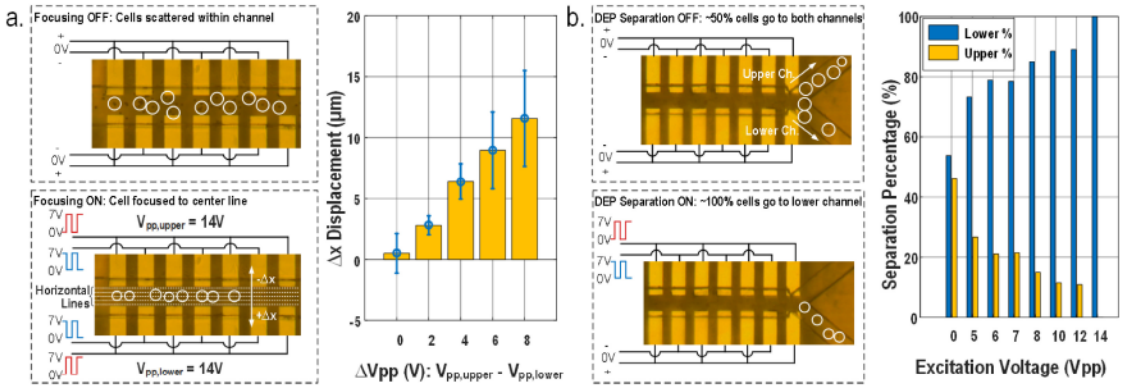

Fig. 22. DEP focusing performance characterization. (a) Focusing performance is quantified by measuring lateral positions of the beads/cells passing at the end of the focusing electrodes (bottom left). Best DEP focusing performance can be reached under balanced excitation of 14 Vpp, with cells being center-focused in the channel and an error of 2 μm (right). (b) DEP separation characterization showing by activating only the top electrodes with 14 Vpp nearly 100% of the cells are separated into the correct channel.

demonstrate the capability of the function, that can be optimized further depending on the application of interest.

E. Cell Focusing and Positioning With Engineered Fields

As described in Section II, the chip architecture has the ability to engineer the electric fields within a cell flow to precisely control their positions for sensing and subsequent separation. We characterize this functionality through electronic actuations and calibrating it with the video from the microscope (Fig. 22(a)). The cell focusing performance is then measured by recording the lateral displacements under various excitation conditions of a set of fifty 10 μm polystyrene beads (Sigma-Aldrich Supelco 72986). Fig. 22 summarizes the electronic focusing performance under different excitation voltages at 100 kHz with error bars showing the standard deviations of each measuring set. In summary, the best focusing performance can be achieved under excitation voltage of 14 Vpp on both sides, where a standard deviation of only 2 μm of focusing error is observed. This value corresponds to less than 4% of the electrode separation gap of 50 μm, ensuring a consistent cytometry focusing performance. On the contrary, when cells are off-center focused, they will experience different lateral forces from the side with higher excitation voltages, due to different entry locations. The other side of the electrodes with smaller excitation voltage do not provide enough force to counterbalance the cells, resulting in larger standard deviations in measurement (Fig. 22(a)). The proposed implementation significantly improves over the prior works that rely on hydrodynamic focusing that requires separate external pneumatic pumps [37], [38].

Controlling the balance of the excitations on the two sides of electrodes, one can control the lateral displacement of the cells. As shown in Fig. 22(b), when the electrodes are turned off, beads are scattered randomly in the channel (50% going through both channels). As the top excitation voltage increases from 0 V, a larger percentage of cells are separated into the lower channel. At 14 Vpp, nearly 100% of the beads are pushed into the lower channel for 100 measured cells (Fig. 22(b)), demonstrating a very reliable cell separation capability. Therefore, for a 50 μm electrode separation and 100 μm channel width, one-sided voltage excitation above 14 Vpp is preferable.

F. Cytometry Measurement Using Polystyrene Beads

The cytometry impedance measurement is first performed using two types of polystyrene beads: Sigma-Aldrich Supelco 72986 (10 μm) and 74491 (20 μm). First, the beads are diluted from the stock aqueous solution into 0.001$\times$ PBS solution buffer with dilution ratio between 1-0.1%. This ratio is experimentally obtained to prevent clogging in the microfluidic channel while maintaining the best measurement visuals under microscope [53].

The diluted beads are then injected into the microfluidic channel and controlled electronically for accurate impedance measurements. Fig. 23 demonstrates real-time measurement results of size 10 and 20 μm of beads under roughly 100 μm/s of flow rate. The average peak voltages are measured to be around 2 mV for 10 μm when channeled far away from the TIA input electrodes, and 4 mV when channel closer to TIA input electrodes. In addition, for a 20 μm polystyrene bead size, the signal is significantly larger when comparing against 10 μm, reaching nearly 8 mV of signal. This is close to the expected value, as the signal is proportional to the cubic power of the particle volume. The closeness of the cell flow to the electrodes can be controlled by the set of prior DEP electrodes as described previously. In addition, one can also estimate the velocity of the flow fully electronically by measuring the temporal separation of the peaks of a single bead as it flows through the various electrodes.

To allow real-time separation of the cells based on their sizes, it is possible to create an autonomous feedback control system. This separation requires feedback programming/classification to differentiate waveforms caused by different cell sizes in real-time. On average, the time that takes the cell to pass through one impedance sensor is on the order of 0.3 secs under 160 μm/s. Therefore, the electronic feedback system can be made much faster than the biological time constants, allowing a simple threshold detection algorithm to function robustly.

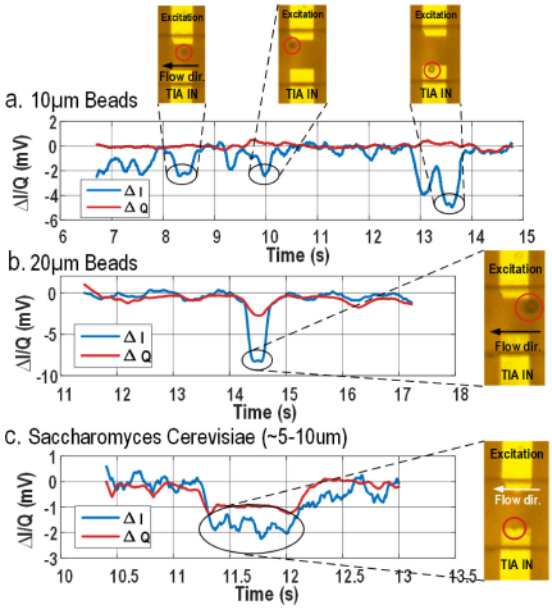

Fig. 23. Cell sensing measurements. (a) Measured real-time sensing results for a 10 μm bead flow. A signal of magnitude $\approx$ 2 mV is observed when the bead flows away from the sensing electrodes. In comparison, the signal is doubled (4 mV), when the bead flows close to the input electrodes. This can be controlled by prior DEP electrodes. (b) For larger beads of size 20 μm, a signal level of 8 mV is measured when the bead flows away from the electrode. (c) Real-time measurement of yeast cell (S. Cerevisiae).

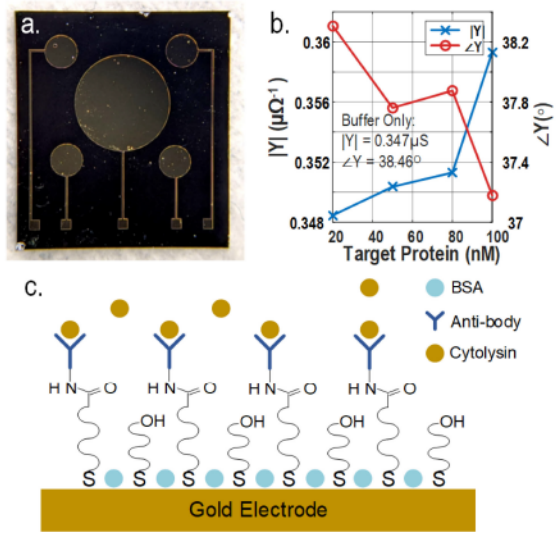

Fig. 24. Label-free bio-molecular sensing measurements. (a) Protein measurement electrode platform with 3 mm diameter for the center excitation electrode and 1 mm diameter for the TIA input electrodes. (b) Measured cytolysin target protein. (c) An illustration of surface chemistry developed for the Cytolysin protein detection, following standard self-assembled monolayer (SAM) bioassay protocol.

G. Cytometry Measurement of Yeast Cell

To demonstrate the cytometric sensing capabilities, we measure the performance with cultured yeast cells (Saccharomyces Cerevisiae). Similar to the previous sample preparation, the yeast cells are suspended in the same 0.001$\times$ PBS solution. The sizes of the yeast cells are in the range of 5-10 μm [60]. Therefore, ensuring consistent focusing of the cell in the channel is a critical aspect in the measurement.

As shown in Fig. 23(c) when the cells are focused close to the TIA input electrodes, the cells demonstrate discernible signal levels ($\approx$ 2 mV of signal), when compared against the solution baseline. The SNR is measured to be around 10 with the yeast cells ($\approx$ 6 μm in diameter) focused close to the edge of the TIA input electrodes. Assuming, the signal level is roughly proportional to the volume of the cell size, the limit-of-detection (LOD) for the cytometry is approximately around 2.7 μm of cell size for SNR $\approx$ 1.

H. Protein Measurement

Finally, protein bioassay measurement capability is also reported in this work. As a proof of concept, the measurement is performed on separate gold electrode platform on silicon substrate, and can be easily integrated in the same glass substrate as the AC osmosis and DEP system electrodes. As shown in Fig. 24(a), the center excitation electrode has a diameter of 3 mm, with four TIA input electrodes (1 mm) located at the corners of the sensor. We then deployed standard label-free self-assembled monolayer (SAM) assay on the custom-fabricated gold electrodes [5], [64]–[67], and the electrode preparations are demonstrated in the following paragraph.

First, the impedance gold electrodes are immersed in acetone, isopropanol (IPA) and Milli-Q water and then sonicating for 3 min. The electrodes were dried with a nitrogen stream and placed in a UV-O3 cleaner (BioForce Nanoscience, USA) for 30 min. Finally, they were rinsed with IPA and dried with nitrogen stream. A mixed self-assembled monolayer (SAM) was formed ex-situ by incubating the gold electrodes overnight at room temperature with a mixed solution of alkanethiols (16-mercaptohexadecanoic acid (MHDA) and 11-mercaptoundecanol (MUOH)) in ethanol. The electrodes were then thoroughly rinsed with ethanol and dried with nitrogen stream [68]–[70].

Before applying the target cytolysin protein, the carboxylic group of MHDA were activated as carbodiimide esters by incubation of a mixed solution of EDC/sulfo-NHS (0.2 M/0.05 M) in MES buffer for one hour, and then rinsed with water and dried. The electrodes were incubated with a solution of antibody (50 μg/mL) in PBS buffer pH 7.4 overnight at room temperature. The electrodes were rinsed with PBS buffer to remove unbound antibody and dried with nitrogen stream. The uncovered gold surface was blocked with a 3% bovine serum albumin (BSA) to avoid non-specific bonding, due to its superior anti-fouling properties. The final surface chemistry is illustrated in Fig. 24(c) after surface functionalization and activation.

We then proceed with the protein measurements with varying target cytolysin concentrations. Fig. 24(b) summarizes the measured admittance w.r.t. different cytolysin concentrations at excitation frequency of 500 kHz. The non-monotonic decrease for $\angle Y$ at 80 nM is caused by slight movement of droplets on different electrode sensors between experimental trials which

TABLE II
COMPARISONS WITH STATE-OF-THE-ART CMOS IMPEDANCE CELL CYTOMETRY AND PROTEIN SENSING SYSTEMS

	This Work	[38]	[61]	[12], [62]	[63]	[54]
Functionality	**CMOS-driven bulk flow + cell focusing + 16-element impedance sensing (4 cell, 12 protein)**	Pressure-driven flow + 2-element impedance sensing	Pressure-driven flow + 1-element impedance sensing	Pressure-driven flow + 4-element microwave dielectric sensing	Pressure-driven flow + 1-element impedance sensing	Protein + DNA impedance spectroscopy in static well
Process	**65nm LP**	N.A.	0.35μm AMS	65nm	N.A.	0.35μm
Sensor Type	**On-chip TIA + direct conversion**	On-chip TIA + direct conversion	Off-chip TIA + direct conversion	Capacitive + high freq. osc.	Off-chip TIA + external SR844 Lock-in Amp	On-chip TIA + direct conversion
Integrated Bulk Fluid Control	**Yes**	No	No	No	No	No
Cell Focusing Method	**Integrated electronic DEP focusing**	External hydrodynamic focusing	External hydrodynamic focusing	External hydrodynamic focusing	External hydrodynamic focusing (oil)	N.A.
Cell Separation /Actuation	**Integrated CMOS-driven DEP separation**	No	Externally-driven DEP separation	No	No	N.A.
Integrated Molecular Sensing	**Yes**	No	No	No	No	No
Power Consumption	**250μW/pixel**	N.A.	N.A.	65mW	N.A. (SR844 Lock-in Amp)	720μW/pixel
Input Referred Noise	**301pArms @ 10Hz**	N.A.	N.A.	N.A.	N.A.	330pArms @ 10Hz
Sensor Dynamic Range	**95dB**	N.A.	N.A.	N.A.	N.A.	97dB
Minimum Cell Detection Size[1] @ S.N.R = 1	**≈ 2.7μm**	≈ 3μm	≈ 2.5μm	≈ 0.3μm	≈ 0.5μm	N.A.
Cell Measurement	**S. cerevisiae**	RBC	S. cerevisiae	Breast cells and leukocytes	E. coli	N.A.

[1]Minimum cell detection size estimated by scaling down the signal and assuming the signal strength is proportional to the cell volume (Sig. $\propto$ diameter^3).

results in a slight drift in impedance signal. This effect can be eliminated through titration of target sensing molecule with a fixed buffer solution on the same electrode sensor, and with more optimized control environment. In summary, the Fig. 24(b) demonstrates the lowest detection concentration at 20 nM when comparing against the solution baseline.

Finally, the performance for the proposed system is summarized in Table II against other state-of-the-art CMOS cytometry/protein biosensor. In particular, this is the first work, to the best of authors' knowledge, that integrates the functionalities of pneumatic-free bulk fluid processing along with microfluidic cytometry and protein sensing in a single battery powered handheld device.

VI. CONCLUSION

In conclusion, we present an approach to combine CMOS-based electrokinetic microfluidics with multi-modal cytometry and protein bioassay sensing array platform for POC applications. Specifically, we focus on realizing pneumatic-free microfluidic drivers with integrated cell actuation and impedance sensing capabilities for both cytometry and label-free protein sensing that are compatible with standard bioassay protocols. We showed AC-osmotic bulk fluid flows with optimized electrode geometries and dynamic engineering of electric fields to precisely control, sense and separate cells for cytometry. We demonstrated 16-element impedance spectroscopic receivers on-chip for real-time cell sensing and protein assays. The approaches can be further optimized to yield better performance, but the presented sensing platform demonstrates a pathway toward pneumatic-free complex biosensing platforms and ultra-miniaturization for in-vitro and in-vivo applications.

ACKNOWLEDGMENT

The authors would like to thank Princeton Catalysis Program, NSF and DARPA for funding support and technical discussions among the IMRL group members at Princeton University.

REFERENCES

[1] J. R. Choi, "Development of point-of-care biosensors for COVID-19," *Front. Chem.*, vol. 8, 2020, Art. no. 517.

[2] T. Frank and S. Tay, "Flow-switching allows independently programmable, extremely stable, high-throughput diffusion-based gradients," *Lab Chip*, vol. 13, no. 7, pp. 1273–1281, 2013.

[3] T. P. Hunt, D. Issadore, and R. M. Westervelt, "Integrated circuit/microfluidic chip to programmably trap and move cells and droplets with dielectrophoresis," *Lab Chip*, vol. 8, no. 1, pp. 81–87, 2008.

[4] C. Zhu, Y. Wen, T. Liu, H. Yang, and K. Sengupta, "A packaged ingestible bio-pill with 15-pixel multiplexed fluorescence nucleic-acid sensor and bi-directional wireless interface for in-vivo bio-molecular sensing," in *Proc. IEEE Symp. VLSI Circuits*, 2020, pp. 1–2.

[5] L. Hong, H. Li, H. Yang, and K. Sengupta, "Fully integrated fluorescence biosensors on-chip employing multi-functional nanoplasmonic optical structures in CMOS," *IEEE J. Solid-State Circuits*, vol. 52, no. 9, pp. 2388–2406, Sep. 2017.

[6] T. Chi *et al.*, "A multi-modality CMOS sensor array for cell-based assay and drug screening," *IEEE Trans. Biomed. Circuits Syst.*, vol. 9, no. 6, pp. 801–814, Dec. 2015.

[7] A. Manickam *et al.*, "A fully integrated CMOS fluorescence biochip for DNA and RNA testing," *IEEE J. Solid-State Circuits*, vol. 52, no. 11, pp. 2857–2870, Nov. 2017.

[8] D. Jung *et al.*, "A CMOS 21 952-pixel multi-modal cell-based biosensor with four-point impedance sensing for holistic cellular characterization," *IEEE J. Solid-State Circuits*, vol. 56, no. 8, pp. 2438–2451, Aug. 2021.

[9] J. S. Park *et al.*, "1024-pixel CMOS multimodality joint cellular sensor/stimulator array for real-time holistic cellular characterization and cell-based drug screening," *IEEE Trans. Biomed. Circuits Syst.*, vol. 12, no. 1, pp. 80–94, Feb. 2018.

[10] D. H. Ta-chien, S. Sorgenfrei, P. Gong, R. Levicky, and K. L. Shepard, "A 0.18 μm CMOS array sensor for integrated time-resolved fluorescence detection," *IEEE J. Solid-State Circuits*, vol. 44, no. 5, pp. 1644–1654, May 2009.

[11] H. Li, X. Liu, L. Li, X. Mu, R. Genov, and A. J. Mason, "CMOS electrochemical instrumentation for biosensor microsystems: A review," *Sensors*, vol. 17, no. 1, 2017, Art. no. 74.

[12] J.-C. Chien, A. Ameri, E.-C. Yeh, A. N. Killilea, M. Anwar, and A. M. Niknejad, "A high-throughput flow cytometry-on-a-CMOS platform for single-cell dielectric spectroscopy at microwave frequencies," *Lab Chip*, vol. 18, no. 14, pp. 2065–2076, 2018.

[13] H. Tang *et al.*, "2D magnetic sensor array for real-time cell tracking and multi-site detection with increased robustness and flow-rate," in *Proc. IEEE Custom Integr. Circuits Conf.*, 2019, pp. 1–4.

[14] C. Steiger, A. Abramson, P. Nadeau, A. P. Chandrakasan, R. Langer, and G. Traverso, "Ingestible electronics for diagnostics and therapy," *Nature Rev. Mater.*, vol. 4, no. 2, pp. 83–98, 2019.

[15] H. Norian, R. M. Field, I. Kymissis, and K. L. Shepard, "An integrated CMOS quantitative-polymerase-chain-reaction lab-on-chip for point-of-care diagnostics," *Lab Chip*, vol. 14, no. 20, pp. 4076–4084, 2014.

[16] X. Huang *et al.*, "A surface acoustic wave pumped lensless microfluidic imaging system for flowing cell detection and counting," *IEEE Trans. Biomed. Circuits Syst.*, vol. 11, no. 6, pp. 1478–1487, Dec. 2017.

[17] H. A. Wake and M. A. Brooke, "Low voltage electrophoresis on a CMOS chip," in *Proc. 50th Midwest Symp. Circuits Syst.*, 2007, pp. 1042–1045.

[18] Y. Yamaji, K. Nakazato, and K. Niitsu, "Sub-1-V CMOS-based electrophoresis using electroless gold plating for small-form-factor biomolecule manipulation," *IEICE Trans. Electron.*, vol. 100, no. 6, pp. 592–596, 2017.

[19] C. Zhu, J. Maldonado, H. Tang, S. Venkatesh, and K. Sengupta, "CMOS-driven pneumatic-free scalable microfluidics and fluid processing with label-free cellular and bio-molecular sensing capability for an end-to-end point-of-care system," in *Proc. IEEE Int. Solid-State Circuits Conf.*, 2021, vol. 64, pp. 278–280.

[20] J. Mok, M. N. Mindrinos, R. W. Davis, and M. Javanmard, "Digital microfluidic assay for protein detection," *Proc. Nat. Acad. Sci., USA*, vol. 111, no. 6, pp. 2110–2115, 2014.

[21] M. Selmi and H. Belmabrouk, "AC electroosmosis effect on microfluidic heterogeneous immunoassay efficiency," *Micromachines*, vol. 11, no. 4, 2020, Art. no. 342.

[22] M. Z. Bazant and T. M. Squires, "Induced-charge electrokinetic phenomena," *Curr. Opin. Colloid Interface Sci.*, vol. 15, no. 3, pp. 203–213, 2010.

[23] Y. Song *et al.*, "AC electroosmosis-enhanced nanoplasmofluidic detection of ultralow-concentration cytokine," *Nano Lett.*, vol. 17, no. 4, pp. 2374–2380, 2017.

[24] T. M. Squires and M. Z. Bazant, "Induced-charge electro-osmosis," *J. Fluid Mechanics*, vol. 509, pp. 217–252, 2004.

[25] R. Rajagopalan, *Principles of Colloid and Surface Chemistry, Revised and Expanded*. Boca Raton, FL, USA: CRC Press, 2016.

[26] G. M. Kontogeorgis, B. Maribo-Mogensen, and K. Thomsen, "The debye-hückel theory and its importance in modeling electrolyte solutions," *Fluid Phase Equilibria*, vol. 462, pp. 130–152, 2018.

[27] N. Islam, "AC electroosmosis for lab-on-a-chip applications," Ph.D. Thesis, Dept. Elect. Comput. Eng., The Univ. Tennessee, Knoxville, TN, USA, 2007.

[28] A. Ajdari, "Pumping liquids using asymmetric electrode arrays," *Phys. Rev. E*, vol. 61, no. 1, 2000, Art. no. R45.

[29] V. Studer, A. Pépin, Y. Chen, and A. Ajdari, "An integrated ac electrokinetic pump in a microfluidic loop for fast and tunable flow control," *Analyst*, vol. 129, no. 10, pp. 944–949, 2004.

[30] Q. Lang, Y. Wu, Y. Ren, Y. Tao, L. Lei, and H. Jiang, "Ac electrothermal circulatory pumping chip for cell culture," *ACS Appl. Mater. Interfaces*, vol. 7, no. 48, pp. 26792–26801, 2015.

[31] M. Mpholo, C. Smith, and A. Brown, "Low voltage plug flow pumping using anisotropic electrode arrays," *Sensors Actuators B: Chem.*, vol. 92, no. 3, pp. 262–268, 2003.

[32] A. Brown, C. Smith, and A. Rennie, "Pumping of water with ac electric fields applied to asymmetric pairs of microelectrodes," *Phys. Rev. E*, vol. 63, no. 1, 2000, Art. no. 016305.

[33] M. Z. Bazant and Y. Ben, "Theoretical prediction of fast 3D AC electro-osmotic pumps," *Lab Chip*, vol. 6, no. 11, pp. 1455–1461, 2006.

[34] J. P. Urbanski, T. Thorsen, J. A. Levitan, and M. Z. Bazant, "Fast AC electro-osmotic micropumps with nonplanar electrodes," *Appl. Phys. Lett.*, vol. 89, no. 14, 2006, Art. no. 143508.

[35] C.-C. Huang, M. Z. Bazant, and T. Thorsen, "Ultrafast high-pressure AC electro-osmotic pumps for portable biomedical microfluidics," *Lab Chip*, vol. 10, no. 1, pp. 80–85, 2010.

[36] Y. Senousy and C. Harnett, "Fast three dimensional AC electro-osmotic pumps with nonphotolithographic electrode patterning," *Biomicrofluidics*, vol. 4, no. 3, 2010, Art. no. 036501.

[37] J.-C. Chien, A. Ameri, E.-C. Yeh, A. N. Killilea, M. Anwar, and A. M. Niknejad, "A high-throughput flow cytometry-on-a-CMOS platform for single-cell dielectric spectroscopy at microwave frequencies," *Lab Chip*, vol. 18, pp. 2065–2076, 2018.

[38] K.-H. Lee, J. Nam, S. Choi, H. Lim, S. Shin, and G.-H. Cho, "A CMOS impedance cytometer for 3D flowing single-cell real-time analysis with $\Delta\Sigma$ error correction," in *Proc. IEEE Int. Solid-State Circuits Conf.*, 2012, pp. 304–306.

[39] A. Valero, T. Braschler, and P. Renaud, "A unified approach to dielectric single cell analysis: Impedance and dielectrophoretic force spectroscopy," *Lab Chip*, vol. 10, no. 17, pp. 2216–2225, 2010.

[40] K. Khoshmanesh, S. Nahavandi, S. Baratchi, A. Mitchell, and K. Kalantar-zadeh, "Dielectrophoretic platforms for bio-microfluidic systems," *Biosensors Bioelectron.*, vol. 26, no. 5, pp. 1800–1814, 2011.

[41] K. Park, S. Kabiri, and S. Sonkusale, "Dielectrophoretic lab-on-CMOS platform for trapping and manipulation of cells," *Biomed. Microdevices*, vol. 18, no. 1, 2016, Art. no. 6.

[42] N.-C. Chen, C.-H. Chen, M.-K. Chen, L.-S. Jang, and M.-H. Wang, "Single-cell trapping and impedance measurement utilizing dielectrophoresis in a parallel-plate microfluidic device," *Sensors Actuators B: Chem.*, vol. 190, pp. 570–577, 2014.

[43] N. Demierre, T. Braschler, R. Muller, and P. Renaud, "Focusing and continuous separation of cells in a microfluidic device using lateral dielectrophoresis," *Sensors Actuators B: Chem.*, vol. 132, no. 2, pp. 388–396, 2008.

[44] M. Evander, A. J. Ricco, J. Morser, G. T. Kovacs, L. L. Leung, and L. Giovangrandi, "Microfluidic impedance cytometer for platelet analysis," *Lab Chip*, vol. 13, no. 4, pp. 722–729, 2013.

[45] C.-H. Lin, G.-B. Lee, L.-M. Fu, and B.-H. Hwey, "Vertical focusing device utilizing dielectrophoretic force and its application on microflow cytometer," *J. Microelectromech. Syst.*, vol. 13, no. 6, pp. 923–932, 2004.

[46] N. Manaresi *et al.*, "A CMOS chip for individual cell manipulation and detection," *IEEE J. Solid-State Circuits*, vol. 38, no. 12, pp. 2297–2305, Dec. 2003.

[47] K. Mohammad, D. A. Buchanan, K. Braasch, M. Butler, and D. J. Thomson, "CMOS single cell dielectrophoresis cytometer," *Sensors Actuators B: Chem.*, vol. 249, pp. 246–255, 2017.

[48] J. Voldman, M. Toner, M. L. Gray, and M. A. Schmidt, "A dielectrophoresis-based array cytometer," in *Transducers' 01 Eurosensors XV*. Berlin, Germany: Springer, 2001, pp. 322–325.

[49] A. Ameri, L. Zhang, A. Gharia, M. Anwar, and A. M. Niknejad, "Dielectrophoretic-assisted biosensor for single-cell characterization at mmWave frequencies in CMOS 28 nm technology," in *Proc. 20th Int. Conf. Solid-State Sensors, Actuators Microsyst. Eurosensors XXXIII*, 2019, pp. 174–177.
[50] A. Ameri, L. Zhang, A. Gharia, A. M. Niknejad, and M. Anwar, "A 114 GHz biosensor with integrated dielectrophoresis for single cell characterization," in *Proc. Symp. VLSI Circuits*, 2019, pp. C314–C315.
[51] G. Mernier, E. Duqi, and P. Renaud, "Characterization of a novel impedance cytometer design and its integration with lateral focusing by dielectrophoresis," *Lab Chip*, vol. 12, no. 21, pp. 4344–4349, 2012.
[52] N. Demierre, T. Braschler, P. Linderholm, U. Seger, H. Van Lintel, and P. Renaud, "Characterization and optimization of liquid electrodes for lateral dielectrophoresis," *Lab Chip*, vol. 7, no. 3, pp. 355–365, 2007.
[53] L. Wang, L. A. Flanagan, N. L. Jeon, E. Monuki, and A. P. Lee, "Dielectrophoresis switching with vertical sidewall electrodes for microfluidic flow cytometry," *Lab Chip*, vol. 7, no. 9, pp. 1114–1120, 2007.
[54] A. Manickam, A. Chevalier, M. McDermott, A. D. Ellington, and A. Hassibi, "A CMOS electrochemical impedance spectroscopy (EIS) biosensor array," *IEEE Trans. Biomed. Circuits Syst.*, vol. 4, no. 6, pp. 379–390, Dec. 2010.
[55] P. Xie *et al.*, "Real time cytokine quantification in wound fluid samples using nanowell impedance sensing," in *Proc. 21st Int. Conf. Solid-State Sensors, Actuators Microsyst.*, 2021, pp. 779–782.
[56] S. R. Mahmoodi *et al.*, "Single-step label-free nanowell immunoassay accurately quantifies serum stress hormones within minutes," *Sci. Adv.*, vol. 7, no. 27, 2021, Art. no. eabf4401.
[57] S. Pashmineh and D. Killat, "Self-biasing high-voltage driver based on standard CMOS with an adapted level shifter for a wide range of supply voltages," in *Proc. Nordic Circuits Syst. Conf.: NORCHIP Int. Symp. System-on-Chip*, 2015, pp. 1–4.
[58] S. Franco, *Design With Operational Amplifiers and Analog Integrated Circuits*, vol. 1988. New York, NY, USA: McGraw-Hill, 2002.
[59] B. Razavi, *Design of Analog CMOS Integrated Circuits*. New York, NY, USA: McGraw-Hill Education, 1st ed., 2000.
[60] H. Feldmann, *Yeast: Molecular and Cell Biology*. Hoboken, NJ, USA: John Wiley & Sons, Inc., 2011.
[61] M. Carminati, G. Ferrari, M. D. Vahey, J. Voldman, and M. Sampietro, "Miniaturized impedance flow cytometer: Design rules and integrated readout," *IEEE Trans. Biomed. Circuits Syst.*, vol. 11, no. 6, pp. 1438–1449, Dec. 2017.
[62] J.-C. Chien and A. M. Niknejad, "Oscillator-based reactance sensors with injection locking for high-throughput flow cytometry using microwave dielectric spectroscopy," *IEEE J. Solid-State Circuits*, vol. 51, no. 2, pp. 457–472, Feb. 2016.
[63] C. Bernabini, D. Holmes, and H. Morgan, "Micro-impedance cytometry for detection and analysis of micron-sized particles and bacteria," *Lab Chip*, vol. 11, no. 3, pp. 407–412, 2011.
[64] G. A. López-Muñoz *et al.*, "Gold/silver/gold trilayer films on nanostructured polycarbonate substrates for direct and label-free nanoplasmonic biosensing," *J. Biophoton.*, vol. 11, no. 8, 2018, Art. no. e201800043.
[65] G. A. López-Muñoz *et al.*, "A label-free nanostructured plasmonic biosensor based on Blu-ray discs with integrated microfluidics for sensitive biodetection," *Biosensors Bioelectron.*, vol. 96, pp. 260–267, 2017.
[66] L. Hong, S. McManus, H. Yang, and K. Sengupta, "A fully integrated CMOS fluorescence biosensor with on-chip nanophotonic filter," in *Proc. Symp. VLSI Circuits*, 2015, pp. C206–C207.
[67] C. Zhu, L. Hong, H. Yang, and K. Sengupta, "Ingestible bioelectronics: A packaged, bio-molecular, fluorescence-based sensor array with ultra-low-power wireless interface," in *Proc. IEEE MTT-S Int. Microw. Symp.*, 2019, pp. 212–215.
[68] L. Hong, H. Li, H. Yang, and K. Sengupta, "Integrated angle-insensitive nanoplasmonic filters for ultraminiaturized fluorescence microarray in a 65 nm digital cmos process," *ACS Photon.*, vol. 5, no. 11, pp. 4312–4322, 2018.
[69] L. Hong, H. Li, H. Yang, and K. Sengupta, "Nano-plasmonics and electronics co-integration in CMOS enabling a pill-sized multiplexed fluorescence microarray system," *Biomed. Opt. Exp.*, vol. 9, no. 11, pp. 5735–5758, 2018.
[70] K. Sengupta, L. Hong, C. Zhu, and X. Lu, "Visible and near-IR nano-optical components and systems in CMOS," *IEEE Open J. Solid-State Circuits Soc.*, vol. 1, pp. 247–262, 2021.

Chengjie Zhu (Graduate Student Member, IEEE) received the B.S. degree in electrical engineering from the Georgia Institute of Technology, Atlanta, GA, USA, in 2016. In Spring 2017, he joined Prof. Kaushik Sengputa's Research Group. His current research interests include designing low-power and sensitive circuits and systems based on CMOS process, developing miniaturized and wireless bio-sensing platforms for in-vitro and in-vivo applications. He was awarded twice with PURA Undergraduate Research Award and had a few publications during his undergraduate years, including IEEE TRANSACTIONS ON BIOMEDICAL CIRCUITS AND SYSTEMS (TBIOCAS), VLSI Technology Circuits Symposium and Biomedical Engineering Society (BMES).

Jesus Maldonado received the Ph.D. degree in biotechnology from the Catalan Institute of Nanoscience and Nanotechnology, Universitat Autonoma de Barcelona, Bellaterra, Spain, in 2017, under the supervision of Prof. Laura Lechuga, and the M.S. degree in micro and nanosystems with Research Center on Micro and Nanotechnology, Veracruz University, Xalapa, Mexico. In 2019, he joined Integrated Micro-systems Research Lab, Princeton University, Princeton, NJ, USA, as a Postdoctoral Research Scientist. His current research interests include Lab-on-a-chip biosensing, nano-biotechnology, bio-mems, and bioanalytical applications.

Kaushik Sengupta (Senior Member, IEEE) received the B.Tech. and M.Tech. degrees in electronics and electrical communication engineering from the Indian Institute of Technology Kharagpur, Kharagpur, India, in 2007, and the M.S. and Ph.D. degrees in electrical engineering from the California Institute of Technology (Caltech), Pasadena, CA, USA, in 2008 and 2012, respectively. In 2013, he joined as a Faculty Member the Department of Electrical and Computer Engineering, Princeton University, Princeton, NJ, USA, where he is currently an Associate Professor and the Director of Graduate Studies. His current research interests include high-frequency ICs, electromagnetics, and optics for various applications in sensing, imaging, and high-speed communication. Dr. Sengupta was the recipient of the DARPA Young Faculty Award in 2018, Bell Labs Prize in 2017, Young Investigator Program Award from the Office of Naval Research in 2017, E. Lawrence Keys, Jr. Emerson Electric Co. Junior Faculty Award from the Princeton School of Engineering and Applied Science in 2018, and Excellence in Teaching Award in 2018 nominated by the Undergraduate and Graduate Student Council in the Princeton School of Engineering and Applied Science. He was the recipient of the Prime Minister Gold Medal Award from IIT Kharagpur in 2007, Charles Wilts Prize in 2013 from Electrical Engineering at Caltech for the best Ph.D. thesis, and inaugural Young Alumni Achievement Award from IIT Kharagpur in 2018. He was the co-recipient of the IEEE RFIC Symposium Best Student Paper Award in 2012 and 2015 Microwave Prize from the IEEE Microwave Theory and Techniques Society. He is the Sub-Committee Chair on Emerging Technologies in IEEE Custom Integrated Circuits Conference (CICC), in the Technical Program Committee in IEEE International Microwave Symposium, and was the Guest Editor of IEEE JOURNAL OF SOLID-STATE CIRCUITS. He is a Member of the MTT-4 Committee on Terahertz Technology and was a Distinguished Lecturer of the IEEE Solid-State Circuits Society from 2019 to 2020. He is currently a Distinguished Lecturer of the IEEE Microwave Theory and Techniques from 2021 to 2023. He was the recipient of the 2021 IEEE Microwave Theory and Techniques Outstanding Young Engineer Award.